Cell Reports

Intraflagellar Transport Complex B Proteins Regulate the Hippo Effector Yap1 during Cardiogenesis

Graphical Abstract

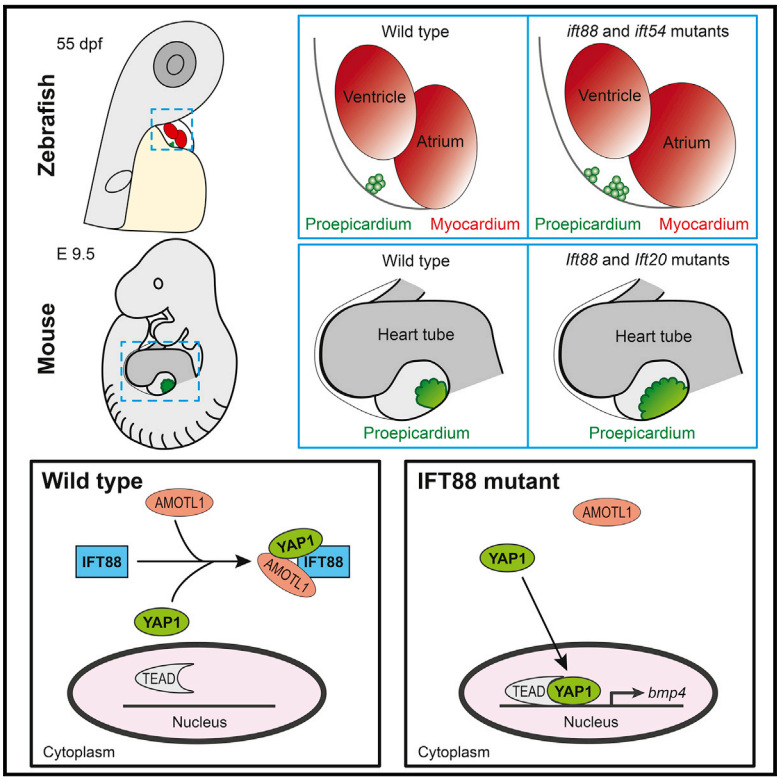

Highlights

- IFT proteins restrict proepicardial and myocardial development
- IFT proteins act independently of primary cilia in this process
- IFT proteins modulate BMP signaling by tuning Yap1-Tead activity
- IFT88 and IFT20 interact with YAP1 in the cytoplasm to set Yap1-Tead activity

Authors

Marina Peralta, Laia Ortiz Lopez, Katerina Jerabkova, ..., Benedicte Delaval, Sigolène M. Meilhac, Julien Vermot

Correspondence

jvermot@imperial.ac.uk

In Brief

Peralta et al. show that intraflagellar transport (IFT) complex B proteins (Ift88, Ift54, and Ift20) modulate the Hippo pathway effector Yap1 in zebrafish and mouse. This cytoplasmic interaction is key to restrict proepicardial and myocardial development.

Peralta et al., 2020, Cell Reports *32*, 107932
July 21, 2020
https://doi.org/10.1016/j.celrep.2020.107932

CellPress

Cell Reports

CellPress
OPEN ACCESS

Report

Intraflagellar Transport Complex B Proteins Regulate the Hippo Effector Yap1 during Cardiogenesis

Marina Peralta,[1,2,3,4] Laia Ortiz Lopez,[1,2,3,4,13] Katerina Jerabkova,[1,2,3,4,13] Tommaso Lucchesi,[5,6,7,13] Benjamin Vitre,[8] Dong Han,[5,6] Laurent Guillemot,[5,6] Chaitanya Dingare,[9] Izabela Sumara,[1,2,3,4] Nadia Mercader,[10,11] Virginie Lecaudey,[9] Benedicte Delaval,[8] Sigolène M. Meilhac,[5,6] and Julien Vermot[1,2,3,4,7,12,14,*]

[1]Institut de Génétique et de Biologie Moléculaire et Cellulaire, Illkirch, France
[2]Centre National de la Recherche Scientifique, UMR7104, Illkirch, France
[3]Institut National de la Santé et de la Recherche Médicale, U964, Illkirch, France
[4]Université de Strasbourg, Illkirch, France
[5]*Imagine*–Institut Pasteur, Laboratory of Heart Morphogenesis, Paris, France
[6]INSERM UMR1163, Université Paris Descartes, Paris, France
[7]Sorbonne Université, Collège Doctoral, F-75005, Paris, France
[8]Centre de Recherche en Biologie Cellulaire de Montpellier (CRBM), CNRS, Université de Montpellier, Montpellier, France
[9]Institute for Cell Biology and Neurosciences, Goethe University of Frankfurt, Frankfurt, Germany
[10]Institute of Anatomy, University of Bern, Bern, Switzerland
[11]Centro Nacional de Investigaciones Cardiovasculares (CNIC), Madrid, Spain
[12]Department of Bioengineering, Imperial College London, London, UK
[13]These authors contributed equally
[14]Lead Contact
*Correspondence: jvermot@imperial.ac.uk
https://doi.org/10.1016/j.celrep.2020.107932

SUMMARY

Cilia and the intraflagellar transport (IFT) proteins involved in ciliogenesis are associated with congenital heart diseases (CHDs). However, the molecular links between cilia, IFT proteins, and cardiogenesis are yet to be established. Using a combination of biochemistry, genetics, and live-imaging methods, we show that IFT complex B proteins (Ift88, Ift54, and Ift20) modulate the Hippo pathway effector YAP1 in zebrafish and mouse. We demonstrate that this interaction is key to restrict the formation of the proepicardium and the myocardium. *In cellulo* experiments suggest that IFT88 and IFT20 interact with YAP1 in the cytoplasm and functionally modulate its activity, identifying a molecular link between cilia-related proteins and the Hippo pathway. Taken together, our results highlight a noncanonical role for IFT complex B proteins during cardiogenesis and shed light on a mechanism of action for ciliary proteins in YAP1 regulation.

INTRODUCTION

Primary cilia are immotile microtubule-based organelles, well known for being both chemical and/or mechanical sensors (Berbari et al., 2009; Ferreira et al., 2019). Disruption of cilia function causes multiple human syndromes known as ciliopathies (Reiter and Leroux, 2017). Cilia are required for cardiac development and mutations in cilia-related proteins have been linked to congenital heart diseases (CHDs) (Klena et al., 2016; Li et al., 2015; San Agustin et al., 2016; Slough et al., 2008). Nevertheless, the specific role of cilia and cilia-related proteins during cardiogenesis is still unclear.

Intraflagellar transport (IFT) proteins are required for the transport of cilia components along the axoneme and are thus essential for cilia formation and function (Rosenbaum and Witman, 2002). The role of IFT proteins during ciliogenesis is highly conserved across organisms (Taschner et al., 2012). The IFT machinery is composed of two biochemically distinct subcomplexes, IFT-A and IFT-B (Taschner et al., 2012). The IFT complex B member IFT20, which localizes inside the cilium and at the Golgi complex in mammalian cells, participates in the sorting and/or transport of membrane proteins for the cilia (Follit et al., 2006). Within the IFT complex B, IFT20 interacts with IFT54/Elipsa (Omori et al., 2008; Zhu et al., 2017) and IFT88, which is essential for flagellar assembly in *Chlamydomonas* and ciliogenesis in vertebrates (Pazour et al., 2000). Mutations in some IFT proteins have been identified in CHDs (Li et al., 2015). IFT proteins also display noncanonical, cilia-independent functions (Hua and Ferland, 2018; Vertii et al., 2015). IFT88, for example, is needed for spindle orientation and organization, cleavage furrow ingression, or extra centrosome clustering in dividing cells (Delaval et al., 2011; Taulet et al., 2017, 2019; Vitre et al., 2020) and regulates G1-S phase transition in nonciliated cells (Robert et al., 2007). IFT20, together with IFT88 and IFT54, plays a role

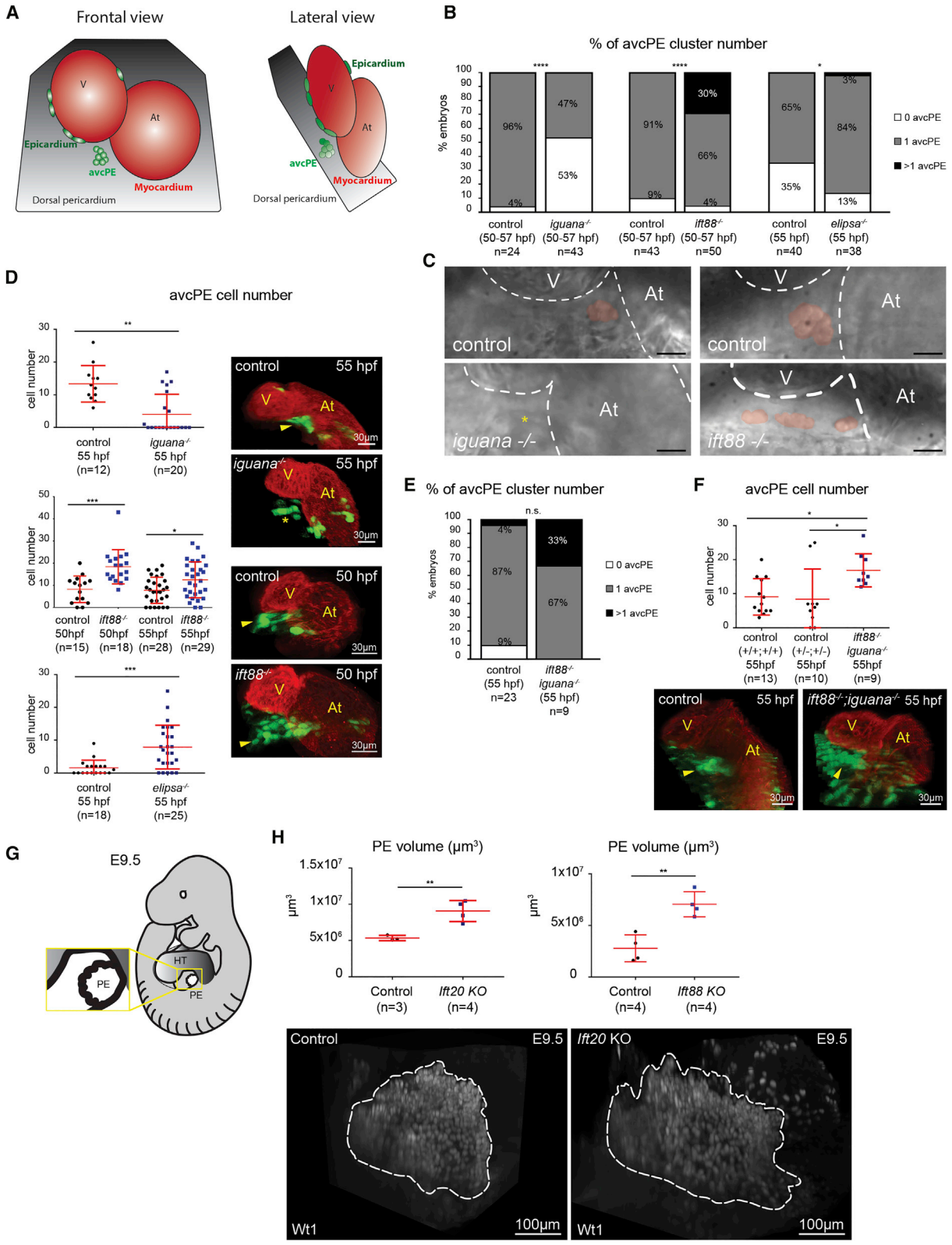

(legend on next page)

in the establishment of the immune synapse in T lymphocytes lacking cilia (Finetti et al., 2009; Galgano et al., 2017). These observations suggest that IFT proteins could play a key role in embryonic cardiogenesis through both cilia-dependent and -independent functions.

The Hippo signaling mediators, YAP1/WWTR1 (TAZ), constitute a key signaling pathway for the regulation of cardiac development (Fukui et al., 2018; Lai et al., 2018; Ragni et al., 2017; Xin et al., 2011) and cardiac regeneration (Bassat et al., 2017; Leach et al., 2017) in vertebrates. For example, YAP1/WWTR1 (TAZ) are required for epicardium and coronary vasculature development (Singh et al., 2016) in mice. In addition, Yap1 signaling has been reported to regulate the number of atrial cardiomyocytes derived from Islet1 (Isl1)-positive (+) secondary heart field (SHF) cells in the zebrafish (Fukui et al., 2018). Changes in cell shape, substrate stiffness, and tension forces activate a phosphorylation-independent YAP1/WWTR1 (TAZ) modulation (Elosegui-Artola et al., 2017), which is mediated by the Motin family (AMOT, AMOTL1, and AMOTL2) (Bratt et al., 2002; Zheng et al., 2009). Motin proteins bind to YAP/WWTR1 (TAZ), sequestering them in the cytoplasm in several cellular contexts (Agarwala et al., 2015; DeRan et al., 2014; Nakajima et al., 2017; Wang et al., 2011; Zhao et al., 2011). While it is known that ciliary proteins from the Nephrocystin family modulate the transcriptional activity of YAP1/WWTR1 (TAZ) (Frank et al., 2013; Grampa et al., 2016; Habbig et al., 2012) and that the Hippo kinases MST1/2-SAV1 promote ciliogenesis (Kim et al., 2014), the connection between the Hippo pathway and cilia function remains unclear.

Cardiogenesis involves an interplay between multiple tissue layers. The epicardium is the outermost layer covering the heart. This cardiac cell layer plays an essential role in myocardial maturation and coronary vessel formation during development (Männer et al., 2005; Moore et al., 1999; Wu et al., 2013) and has a crucial role during regeneration (González-Rosa et al., 2012; Kikuchi and Poss, 2012; Limana et al., 2011). Epicardial cells derive from the proepicardium (PE), an extracardiac transient cluster of heterogeneous cells (Katz et al., 2012). The PE, the sinoatrial node, and the atrial myocardium all derive from the SHF (Buckingham et al., 2005; Mommersteeg et al., 2010; van Wijk et al., 2009). In zebrafish, the transcription factor Isl1 marks a subset of SHF cells that give rise to part of the atrial myocardium (de Pater et al., 2009; Witzel et al., 2012). In mice, the PE is a single cell cluster located close to the venous pole of the heart (Katz et al., 2012), while in zebrafish it is composed of two cell clusters, avcPE (the main source of cells) and vpPE (Peralta et al., 2013). PE cells give rise to the epicardium, part of the coronary vasculature, and intracardiac fibroblasts (Acharya et al., 2012; Katz et al., 2012; Mikawa and Fischman, 1992; Mikawa and Gourdie, 1996). The secreted signaling molecules of the bone morphogenetic protein (BMP) family are indispensable for PE formation (Ishii et al., 2010; Liu and Stainier, 2010; Schlueter et al., 2006).

Despite the increasing evidence for the role of IFT proteins in cell signaling, it has been difficult to pinpoint the exact function of cilia-related proteins outside the cilium. Without this key information, the question of whether cilia-related proteins can affect the developmental program independently of their cilia function remains unresolved. Here, we provide a combination of *in vivo* and *in vitro* analyses of IFT protein function showing that IFT complex B proteins can modulate the Hippo pathway effector Yap1. In particular, we show that IFT88 is required to restrict PE and myocardium development through cytoplasmic activity.

RESULTS

IFT Complex B Proteins Regulate PE Development in Zebrafish and Mouse

Considering the importance of cilia during cardiogenesis, we assessed the role of several IFT complex B proteins during PE development. In order to benefit from live imaging and genetics, we used zebrafish as a model organism. We performed live-imaging focusing on the main PE cell source located near the atrioventricular canal (avcPE) in *ift88* (Tsujikawa and Malicki, 2004) and *elipsa/ift54* (Omori et al., 2008) mutants (Figures 1A–1D). Between 50 and 57 hours post fertilization (hpf), we found that *ift88* mutants display multiple avcPE clusters (either two or three), when controls have only one (Video S1). Using a *wilms tumor 1 a* (*wt1a)* enhancer trap line that marks proepicardial and epicardial cells (*Et(−26.5Hsa.WT1-gata2:EGFP)*^{cn1}; hereafter, *epi:GFP*) (Peralta et al., 2013), we quantified avcPE and epicardial cell number and found that *ift88*$^{-/-}$ have increased avcPE and

Figure 1. IFT Complex B Proteins Regulate Proepicardial Development in Zebrafish and Mice

(A) Schematic representation of the zebrafish heart at 55 hpf in frontal and lateral views. The dorsal pericardium (DP) is shown in gray, the myocardium (myoc) in red, the avcPE in light green, and the epicardial cells in dark green.

(B) Percentage of avcPE cluster number in *iguana* (n = 43), *ift88* (n = 50), and *elipsa/ift54* (n = 38) mutants and their controls (n = 24; n = 43; n = 40, respectively), between 50 and 57 hpf (Mann-Whitney test, *iguana* p value < 0.0001; *ift88* p value < 0.0001; *elipsa* p value, 0.014).

(C) High-speed avcPE imaging (digital red mask to improve visualization) of *iguana* and *ift88* mutants and their control. Scale bars: 20 μm.

(D) Graphs show avcPE cell number quantified on *iguana* (n = 20), *ift88* (n = 18 and 29), and *elipsa* (n = 25) mutants in *epi:GFP* background and their controls (n = 12; n = 15; n = 28 n = 18, respectively) (t test, *iguana* p value, 0.001; *ift88* p value, 0.0002; and p value, 0.015, respectively; *elipsa* p value, 0.0005). 3D projections of whole-mount immunofluorescence (IF) of hearts using anti-myosin heavy chain antibody (MHC) (red) and GFP (green) expression.

(E) Percentage of avcPE cluster number on *iguana*$^{-/-}$, *ift88*$^{-/-}$, *epi:GFP* (n = 9), and controls (n = 23) at 55 hpf (Mann-Whitney test, p value, 0.059).

(F) Graph shows avcPE cell number quantified in wild-type (n = 13), double-heterozygous controls (n = 10), and double *ift88; iguana* mutants (n = 9) (Kruskal-Wallis, p value, 0.014). 3D projections of whole-mount IF of hearts. MHC (red) and GFP (green) expression.

(G) Schematic representation of an E9.5 mouse embryo. Heart tube (HT) in dark gray and PE in white. Section of the PE represented inside the yellow box.

(H) Left-side graph shows quantification of PE volume (in cubic micrometers) in Ift20 KO (n = 4) and control mice (n = 3) (control, 5.35 × 10^6 μm^3 ± 3.63 × 10^5; Ift20 KO, 9.06 × 10^6 μm^3 ± 1.46 × 10^6) (t test, p value, 0.008) and that of *Ift88* KO (n = 4) and control embryo (n = 4) on the right (control, 2.78 × 10^6 μm^3 ± 1.3 × 10^6; *Ift88* KO, 7.05 × 10^6 μm^3 ± 1.2 × 10^6) (t test, p value, 0.003). In the lower panel, 3D projections of whole-mount IF performed on control and *Ift20* KO embryos. PE marked using anti-Wt1 antibody. The white dotted shapes enclose the PE area. In all graphs, red bars indicate mean ± SD. In all panels, ventral views, anterior is to the top. Arrowheads mark avcPE, and asterisk shows lack of avcPE. V, ventricle; At, atrium.

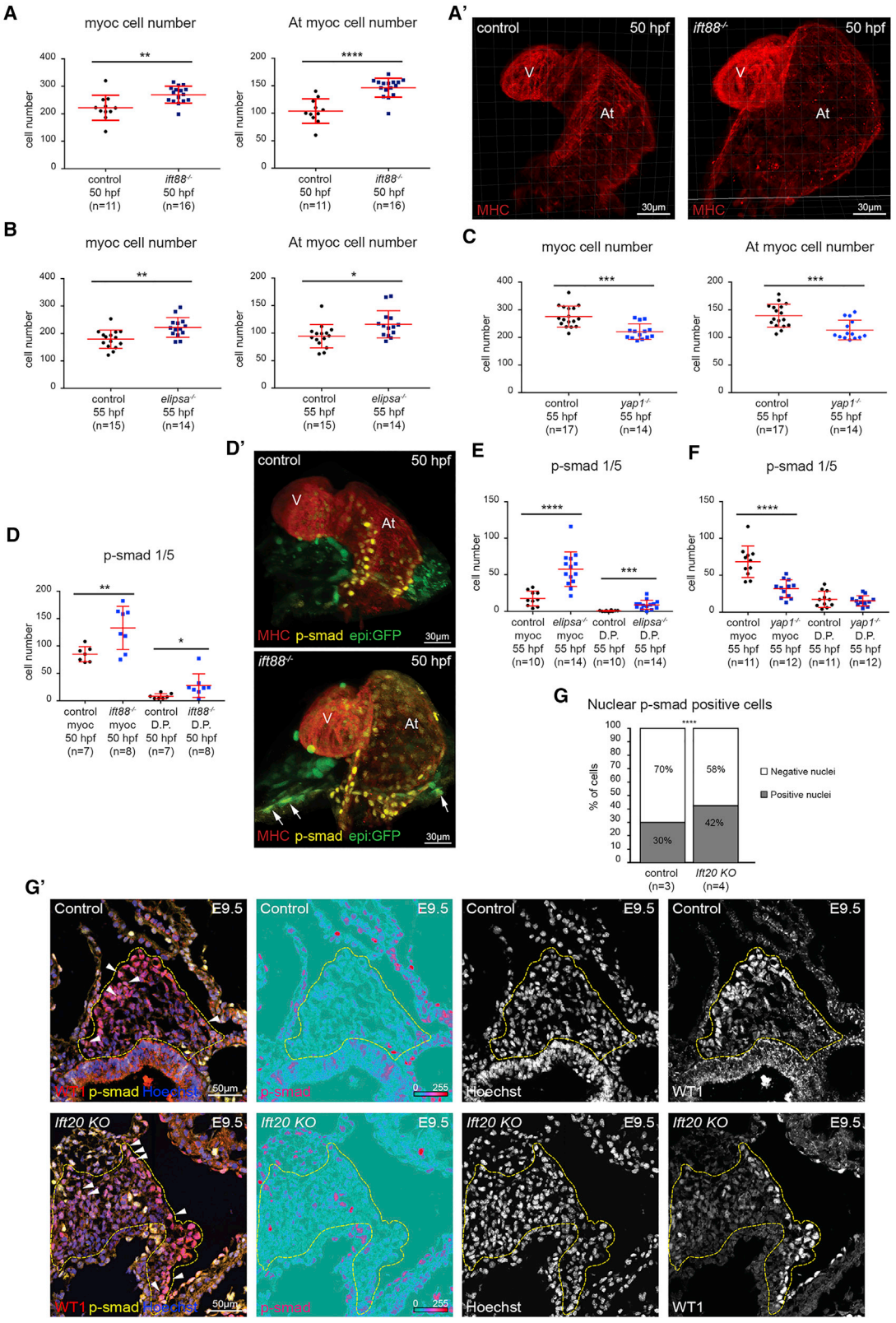

(legend on next page)

epicardial cell numbers compared to their controls at 50 and 55 hpf, respectively (Figures S1B and S2A). Similarly, we found that *elipsa*$^{-/-}$ also showed bigger avcPE compared to controls (Figures S1C and S2A″). Taken together, these data indicate that *ift88* and *elipsa/ift54* are required to restrict PE size.

To determine whether primary cilia are required for PE formation, we took advantage of the *iguana/dzip* (Tay et al., 2010) mutant, a well-established cilia mutant lacking primary cilia (Kim et al., 2010). We confirmed the absence of primary cilia in the pericardial cavity of the *iguana*$^{-/-}$ using the cilia reporter *actb2:Mmu.Arl13b-GFP* (Borovina et al., 2010; Figures S2C–S2E; Video S2). Zebrafish *ift* genes are expressed maternally (Sun et al., 2004; Figure S2E), and complete removal of both zygotic and maternal expression of *ift88* leads to the ablation of primary cilia resembling the *iguana* mutant phenotype (Huang and Schier, 2009). Live imaging revealed that a significant fraction of *iguana* mutants lacked an avcPE between 50 and 57 hpf (Figure 1B; Video S3). At 55 hpf, *iguana*$^{-/-}$ displayed decreased avcPE cell numbers (Figures 1D, S1A, and S2A′). Since the *iguana* mutants presented a phenotype opposite to that of the *ift88* mutants, we analyzed the *ift88*$^{-/-}$*; iguana*$^{-/-}$*; epi:GFP* double mutant to elucidate whether the differences could be due to a new cilia-independent function. The *ift88*$^{-/-}$*; iguana*$^{-/-}$*;* double mutant shows multiple avcPE cluster formation and an increased avcPE cell number, reminiscent of *ift88* loss of function (Figures 1E, 1F, and S1D). We conclude that Ift88 modulates the PE cell number independently of its cilia function.

We assessed whether the role of IFT complex B proteins during PE formation was conserved in mammals. We analyzed the PE in *Ift20* and *Ift88* knockout (KO) mice at mouse embryonic day 9.5 (E9.5) (Figures S3A and S3B). First, we performed immunofluorescence (IF) using an anti-Arl13b antibody to quantify the percentage of ciliated PE cells in *Ift20*, *Ift88* KO, and wild-type mice (Figures S3C–S3C″). We found that, while over 60% of the wild-type PE cells were ciliated, in *Ift88* KO mice only 3% of cells were ciliated and *Ift20* KO embryos lack cilia. We compared the PE volume of *Ift20* and *Ift88* KO mice to their controls, using an anti-Wt1 antibody (a well-established PE marker; Carmona et al., 2001). Mutant embryos showed increased PE volume (Figures 1G and 1H; Videos S5 and S6). These results suggest that IFT protein function is conserved during PE formation in mouse and zebrafish.

To test whether IFT complex B affected other cardiac tissues, we focused on the myocardium. Cell quantification showed increased myocardial cell number in *ift88*$^{-/-}$ compared to their controls at 50 hpf (Figures 2A and 2A′) and 55 hpf (Figure S4A). Interestingly, the increment was mostly affecting the atrium. Similar data were obtained with the *elipsa* mutants at 55 hpf (Figure 2B). We concluded that the absence of IFT complex B proteins also affects the myocardium.

To determine whether Isl1^{+} SHF cells were altered at earlier stages leading to the increment in avcPE and atrial myocardial cells, we quantified Isl1^{+} cells in *ift88* and *amotl2a* mutants at 36 hpf. We did not find differences between *ift88*$^{-/-}$, *amotl2a*$^{-/-}$, and their controls (Figure S1E).

BMP Signaling Is Increased in *ift88*, *elipsa/ift54*, and *Ift20* Mutants during PE Development

As it is known in zebrafish that overexpressing BMP increases PE size (Liu and Stainier, 2010), we investigated whether *ift88* loss influences BMP signaling. We first assessed *bmp4* expression by *in situ* hybridization (ISH) in *ift88* and *elipsa* mutants. We found that *ift88*$^{-/-}$ display ectopic expression of *bmp4* in the dorsal pericardium (DP) at 48 hpf (Figure S4B). To validate that the upregulation is functional *in vivo*, we quantified cellular BMP activity by using p-smad1/5 as a readout and confirmed that the absence of Ift88 leads to increased BMP signaling activity in the DP and myocardium, especially in the venous pole (Figures 2D, 2D′, and S4C). By 55 hpf, *bmp4* expression at the atrioventricular canal myocardium is reduced and the expression at the venous pole is almost undetectable in controls. By contrast, *ift88* mutants presented strong *bmp4* expression in both domains (Figure S4B). Myocardial p-smad1/5 was also increased in *ift88*$^{-/-}$ compared to controls, but not in the DP (Figures

Figure 2. BMP Signaling Is Increased in *ift88*, *elipsa/ift54*, and *Ift20* Mutants

(A) Graphs show total myocardial (myoc) and atrial-myoc cell number quantified in *ift88* (n = 16) mutants and controls (n = 11) at 50 hpf (t test, total myoc p value, 0.0034; atrial myoc p value < 0.0001).

(A′) 3D projections of whole-mount immunofluorescence (IF) of hearts using myosin heavy chain antibody (MHC) (red).

(B) Graphs show total myoc and atrial-myoc cell number quantified in *elipsa* (n = 14) mutants and controls (n = 15) at 55 hpf (t test, total myoc p value, 0.0026; atrial myoc p value, 0.017).

(C) Graphs show total myoc and atrial-myoc cell number quantified in *yap1* (n = 14) mutants and controls (n = 17) at 55 hpf (t test, total myoc p value, 0.0001; atrial myoc p value, 0.0009).

(D) Graph shows number of p-smad1/5^{+} cells in the myoc and dorsal pericardium (DP) quantified in *ift88* mutants (n = 8) and controls (n = 7) at 50 hpf. Myoc (t test, p value, 0.009) and DP (t test, p value, 0.036).

(D′) 3D projections of whole-mount IF of hearts. MHC (red), *epi:GFP* (green), and p-smad1/5 (yellow). Arrows mark dorsal pericardial cells positive for *epi:GFP* and p-smad1/5 (same embryos as in A′).

(E) Graph shows number of p-smad1/5^{+} cells in the myoc and DP quantified in *elipsa* mutants (n = 14) and controls (n = 10) at 55 hpf. Myoc (t test, p value < 0.0001) and DP (t test, p value, 0.0004).

(F) Graph shows number of p-smad1/5^{+} cells in the myoc and DP quantified in *yap1*$^{-/-}$*; tcf21:nls-GFP* (n = 12) and controls (n = 11) at 55 hpf. Myoc (t test, p value < 0.0001) and DP (t test, p value, 0.599).

(G) Graph shows that the percentage of p-smad1/5/9^{+} PE cells is higher in *Ift20* KO (n = 4 embryos: 1,862 nuclei analyzed) compared to control (n = 3 embryos: 1,414 nuclei analyzed) mice (Chi-square test of homogeneity = 51.593; p value, 6.829e-13 on 1 degree of freedom).

(G′) Control and *Ift20* KO IF confocal cryosections labeled with WT1 (red), p-smad1/5/9 (yellow), and Hoechst (blue) at E9.5. Yellow dotted lines enclose the PE area. Arrowheads mark p-smad1/5/9 and Wt1 double-positive cells. Individual channels are displayed for p-smad1/5/9 (signal is shown as ice LUT to facilitate the visualization of signal intensity, where green is the minimum and red is the maximum), Hoechst (white), and WT1 (white). In all graphs, red bars indicate mean ± SD. V, ventricle; At, atrium. Ventral views, anterior is to the top. p-smad, p-smad1/5 in (D′) and p-smad1/5/9 in (G′).

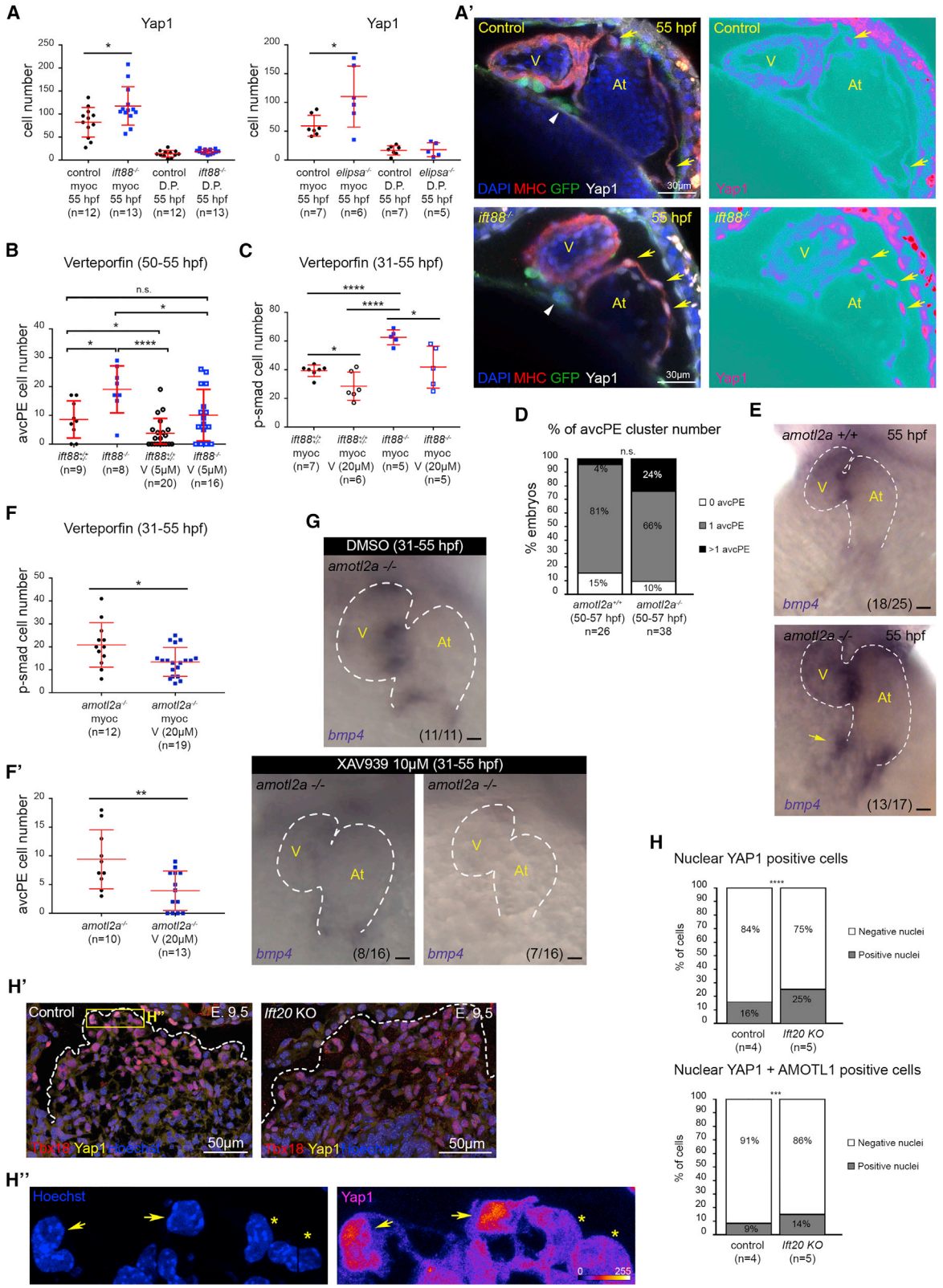

(legend on next page)

S4C and S4D). We reached similar conclusions when analyzing the *elipsa* mutants at 55 hpf (Figures 2E, S4B, and S4C). To confirm that the regulation of BMP signaling by IFT is conserved in vertebrates, we analyzed p-smad1/5/9 in *Ift20* and *Ift88* KO and control mice at E9.5 and found that only the *Ift20* mutants displayed a higher percentage of p-smad^{+} cells compared to controls (Figures 2G, 2G′, and S3D). Together, these results suggest that Ift88 and Ift54 modulate BMP signaling activity in the myocardium and the pericardium of the zebrafish, and that IFT20 plays a similar role in the mouse PE.

Yap1-Tead Activity Is Increased in *ift88*, *elipsa/ift54*, and *Ift20* Mutants during PE Development

Yap1 participates in the regulation of Bmp signaling during SHF development (Fukui et al., 2018). This led us to assess whether Yap1/Wwtr1-Tead is active during PE formation using the *4xGTIIC:d2GFP* reporter line (Miesfeld and Link, 2014). We found that the reporter was active in the PE cluster, myocardium, pericardium, and epicardial cells at 55 hpf (Figure S5A). We performed time-lapse analysis to study the dynamics of Yap1/Wwtr1-Tead activity during PE development (Video S4). GFP quantification in PE and pericardial cells showed higher Yap1/Wwtr1-Tead activity (GFP average intensity) in the PE cells than in the pericardial cells (75% of the embryos) (Figure S5B; Table S1).

To test whether pericardial cells have differential Yap1 activity at earlier stages, before avcPE formation, we analyzed *4xGTIIC:d2GFP* reporter expression at 36 hpf (Figure S5D). We observed that some pericardial cells show stronger GFP intensity (hence higher levels of active Yap1) than others. Consistently with our data at later stages (Video S4; Figure S5B), pericardial cells at the area that will give rise to the avcPE show stronger GFP intensity. Additionally, we obtained similar data with Ctgf antibody, a well-characterized Yap1 target gene (Zhao et al., 2008; Figure S5E).

To test whether the increased avcPE cell number was due to abnormal Yap1 activity, we performed IF to quantify the number of nuclear Yap1^{+} cells in *ift88* and *elipsa* mutants (Figures 3A, 3A′ and S5F–S5G′). At 55 hpf, *ift88*$^{-/-}$ showed more myocardial with nuclear Yap1^{+} cells than controls, especially in the atrium (Figure 3A-A'). Similar data were obtained with the *elipsa* mutants (Figure 3A). To further validate the link between increased PE size and Yap1-Tead activity, we treated the *ift88*$^{-/-}$ with the drug Verteporfin, which binds to YAP and changes its conformation, blocking its interaction with TEAD (Liu-Chittenden et al., 2012). To assess Verteporfin specificity, we performed time-lapse imaging on Verteporfin-treated *4xGTIIC:d2GFP* embryos. We measured the Yap/Wwtr1-Tead activity (GFP average intensity) in the same PE and pericardial cells at several time points: before adding Verteporfin (t0), after 2-h treatment with Verteporfin, and 45 min after washing out (Figure S5C). We found that Yap/Wwtr1-Tead activity is significantly decreased with Verteporfin, confirming the specificity of the drug on the embryo. We next treated *ift88*$^{-/-}$ and control (*ift88*$^{+/+}$ and $^{+/-}$) embryos with Verteporfin (Figure 3B). Control embryos treated with Verteporfin showed smaller avcPE compared to untreated controls.

Figure 3. Yap1-Tead Activity Is Increased in *ift88*, *elipsa/ift54*, and *Ift20* Mutants during Proepicardium Development

(A) Graphs show number of Yap1^{+} cells in the myocardium (myoc) and dorsal pericardium (DP) quantified in *ift88* (n = 13), *elipsa* (n = 6), and their controls (n = 12 and n = 7, respectively). *ift88* mutants show increased Yap1^{+} myoc cell numbers (t test, p value, 0.03) and a tendency toward higher Yap1^{+} DP cell numbers (t test, p value, 0.07). *elipsa* mutants show higher Yap1^{+} myoc cell numbers (t test, p value, 0.036).

(A′) Control and *ift88*$^{-/-}$, *epi:GFP* immunofluorescence (IF) confocal sections labeled with anti-myosin heavy chain antibody (MHC) (red), GFP (green), -Yap1 (white), and DAPI (blue) at 55 hpf. Individual channel is displayed for Yap1 (signal is shown as ice LUT to facilitate the visualization of signal intensity, where green is the minimum and red is the maximum). Yellow arrows mark nuclear Yap1-positive atrial myocardial cells. White arrowheads mark the avcPE.

(B) Graph shows avcPE cell number quantified in control (n = 9), *ift88*$^{-/-}$*; epi:GFP* (n = 8) and Verteporfin (5 μM)-treated *ift88*$^{-/-}$*; epi:GFP* (n = 16) and control (n = 20) embryos. Control embryos treated with Verteporfin showed smaller avcPE compared to untreated controls (t test, p value, 0.04). Verteporfin-treated *ift88*$^{-/-}$*; epi:GFP* embryos presented lower avcPE cell numbers than nontreated *ift88*$^{-/-}$*; epi:GFP* embryos (t test, p value, 0.027). *ift88*$^{-/-}$*; epi:GFP* embryos showed bigger avcPE compared to untreated (t test, p value, 0.01) and treated controls (t test, p value, 0.0001).

(C) Graph shows number of p-smad1/5^{+} cells in the myoc quantified in control (n = 7), *ift88*$^{-/-}$*; epi:GFP* (n = 5), and Verteporfin (20 μM)-treated *ift88*$^{-/-}$*; epi:GFP* (n = 5) and control (n = 6) embryos from 31 to 55 hpf. Control embryos treated with Verteporfin showed decreased p-smad1/5^{+} cell numbers compared to untreated controls (t test, p value, 0.0219). Verteporfin-treated *ift88*$^{-/-}$*; epi:GFP* embryos presented less p-smad1/5^{+} cells than non-treated *ift88*$^{-/-}$*; epi:GFP* embryos (t test, p value, 0.0173). *ift88*$^{-/-}$*; epi:GFP* embryos showed more p-smad1/5^{+} cells compared to untreated (t test, p value < 0.0001) and treated controls (t test, p value < 0.0001).

(D) Percentage of avcPE cluster number in *amotl2a*$^{+/+}$ (n = 26) and *amotl2a*$^{-/-}$ (n = 38) embryos between 50 and 57 hpf (Mann-Whitney test, p value, 0.08).

(E) Whole-mount bmp4 *in situ* hybridization (ISH) in *amotl2a*$^{+/+}$ (n = 18/25) and *amotl2a*$^{-/-}$ (n = 13/17) embryos (55 hpf). Yellow arrow shows bmp4 overexpression. Scale bars: 20 μm.

(F) Graph shows number of p-smad1/5^{+} cells in the myoc quantified in Verteporfin (20 μM)-treated *amotl2a*$^{-/-}$ (n = 19) embryos from 31 to 55 hpf and untreated *amotl2a*$^{-/-}$ (n = 12) embryos. Treated embryos showed decreased p-smad1/5^{+} cell numbers compared to untreated ones (t test, p value, 0.0148).

(F′) Graph shows avcPE cell number quantified in Verteporfin (20 μM)-treated *amotl2a*$^{-/-}$ (n = 13) embryos from 31 to 55 hpf and untreated *amotl2a*$^{-/-}$ (n = 10) embryos. Treated embryos showed decreased avcPE cell numbers compared to untreated ones (t test, p value, 0.0059).

(G) Whole-mount bmp4 ISH in XAV939 (10 μM)-treated *amotl2a*$^{-/-}$ (n = 16) from 31 to 55 hpf and untreated embryos (n = 11). Treated embryos showed either decreased (n = 8/16) or absent (n = 7/16) bmp4 expression at the atrioventricular canal myoc and the venous pole. Scale bars: 20 μm.

(H) Graphs show percentages of YAP1^{+} PE cells and double-YAP1-AMOTL1-positive PE cells in *Ift20* KO (n = 5 embryos: 1,196 nuclei analyzed) and control (n = 4 embryos: 929 nuclei analyzed) mice at E9.5. The percentage of nuclear YAP1^{+} PE cells (Chi-square test of homogeneity = 25.354; p value, 4.77E-07 on 1 degree of freedom) and nuclear YAP1-AMOTL1^{+} cells (Chi-square test of homogeneity = 12,025; p value, 5.25E-04 on 1 degree of freedom) were higher in *Ift20* KO than in control mice.

(H′) Control and *Ift20* KO IF confocal sections labeled with TBX18 (red), YAP1 (yellow), and Hoechst (blue) at E9.5. The white dotted lines enclose the PE area.

(H″) Zoomed region shows the difference between nuclear YAP1^{+} cells (yellow arrows) and YAP1-negative cells (yellow asterisks). Hoechst signal (blue) highlights cell nuclei. YAP1 signal is shown as fire LUT to facilitate the visualization of signal intensity, where blue is the minimum and yellow is the maximum. In all graphs, red bars indicate mean ± SD. In all panels, ventral views, anterior is to the top. V, ventricle; At, atrium.

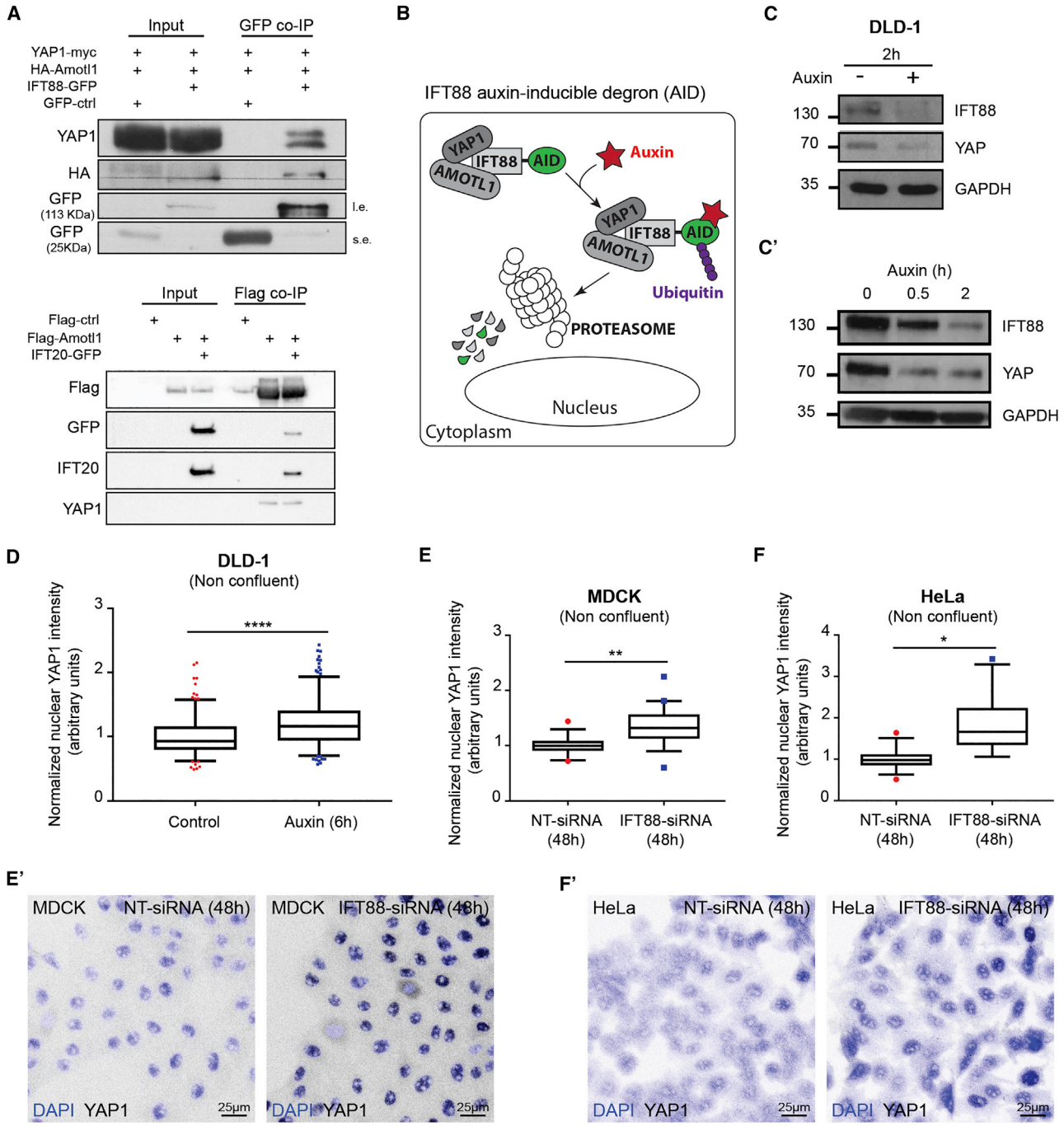

Figure 4. IFT88 and IFT20 Are Physically Associated to YAP1, and IFT88 Modulates YAP1 Activity

(A) Co-IP experiment using HeLa cells transfected with IFT88-GFP, HA-Amotl1, and YAP1-Myc (l.e., long exposure; s.e., short exposure). Co-IP experiment using HEK293 cells transfected with Flag-Amotl1 and IFT20-GFP. Endogenous levels of Yap1 are monitored.

(B) Schematic representation of the IFT88 auxin-inducible degron (AID) system.

(C) Western blot analysis of IFT88 AID DLD-1 cells after 2-h auxin treatment.

(C′) Western blot analysis of IFT88 and YAP1 degradation after auxin treatment (0, 0.5, and 2 h).

(D) Graph shows the increase in normalized YAP1 nuclear signal in cells treated with auxin (6 h) (Mann-Whitney, p value < 0.0001) (controls: 2 replicates, n = 204 cells; Auxin 2 h: 2 replicates, n = 261 cells).

(E) Graph shows the increase in YAP/WWTR1 (TAZ) nuclear signal in IFT88-siRNA (48 h)-treated MDCK cells (n = 5 replicates, average cell number analyzed for each condition = 382; t test, p value, 0.004). Box and whiskers (5th–95th percentile). Outliers are represented as red dots (NT-siRNA) or blue squares (IFT88-siRNA).

(legend continued on next page)

Verteporfin-treated *ift88*$^{-/-}$ embryos presented fewer avcPE cell numbers than nontreated *ift88*$^{-/-}$ embryos. Interestingly, nontreated controls and treated *ift88* mutants did not show significant differences in avcPE cell number. Thus, the increase in avcPE cell number induced in the absence of Ift88 was rescued by Verteporfin treatment. These results suggest that Ift88 requires Yap1 activity to modulate the PE size restriction.

To explore a possible role of Yap1 in the regulation of BMP signaling by IFT, we treated *ift88*$^{-/-}$ and control (*ift88*$^{+/+}$ and $^{+/-}$) embryos with Verteporfin (Figure 3C) and quantified BMP activity. Control embryos treated with Verteporfin showed decreased p-smad1/5^{+} myocardial cell number compared to untreated controls. Verteporfin-treated *ift88*$^{-/-}$ embryos presented fewer p-smad1/5^{+} myocardial cells than nontreated *ift88*$^{-/-}$ embryos. Remarkably, nontreated controls and treated *ift88*$^{-/-}$ did not show significant differences. Thus, the increase in BMP activity induced in the absence of Ift88 was rescued by Verteporfin treatment. Likewise, ISH performed in *elipsa*$^{-/-}$ and control (*elipsa*$^{+/+}$ and $^{+/-}$) embryos treated with Verteporfin displayed decreased *bmp4* expression (Figure S6C). Furthermore, treatment with the drug XAV939, a tankyrase inhibitor that suppressed YAP-TEAD activity (Wang et al., 2015), also led to a reduction of *bmp4* expression (Figure S5H). These results suggest that Ift88 and Ift54 require Yap1 activity to modulate BMP signaling activity in the myocardium of the zebrafish. To confirm the involvement of an increased Yap1 activity in the *ift88*$^{-/-}$ phenotype, we analyzed the avcPE in *angiomotin like 2a* (*amotl2a*) mutants (Figures 3D and 3E). In zebrafish, Amotl2a physically interacts with Yap1 leading to its cytoplasmic retention in a way that *amotl2a* mutants show upregulated Yap1 activity (nuclear Yap1) (Agarwala et al., 2015; Nakajima et al., 2017). Accordingly, *amotl2a*$^{-/-}$ presented multiple avcPE formation and increased *bmp4* expression when compared to *amotl2a*$^{+/+}$ embryos at 55 hpf. When treated with Verteporfin, *amotl2a*$^{-/-}$ showed decreased myocardial p-smad1/5^{+} and avcPE cell numbers compared to untreated *amotl2a*$^{-/-}$ embryos (Figures 3F and 3F′). Likewise, *bmp4* expression at the atrioventricular canal myocardium and at the venous pole were reduced in *amotl2a*$^{-/-}$ embryos treated with XAV939 (Figure 3G). Thus, Verteporfin and XAV939 treatments rescued the increase in BMP signaling induced in the absence of Amotl2a, suggesting it acts through Yap1 activity. We next analyzed the *yap1* mutants (Agarwala et al., 2015). At 55 hpf, *yap1*$^{-/-}$ showed decreased myocardial cell number compared to their controls (Figure 2C). Besides, fewer myocardial cells were p-smad1/5^{+} (Figure 2F). Surprisingly, avcPE cell number was similar between *yap1*$^{-/-}$ and their controls (Figures S2B and S2B′). Altogether, these results suggest that Ift88 and Ift54 modulate BMP signaling activity by tuning Yap1-Tead activity in the myocardium of the zebrafish. To assess whether the upregulation of Yap1 activity observed in IFT zebrafish mutants was conserved in vertebrates, we analyzed YAP1 localization in the PE of *Ift20 KO* and control mice (Figures 3H–3H″). We quantified the proportion of nuclear YAP1^{+} cells (i.e., cells with higher signal intensity inside the nucleus than in the cytoplasm). The percentage of nuclear YAP1^{+} PE cells was higher in *Ift20 KO* than in control mice. In mouse myocardium, YAP1 and AMOTL1 translocate to the nucleus together to modulate cell response (Ragni et al., 2017). To assess AMOTL1 localization in PE cells, we performed AMOTL1 IF. Consistent with the results obtained with an anti-YAP1 antibody, the percentage of nuclear AMOTL1^{+} cells (i.e., cells with higher signal intensity inside the nucleus than in the cytoplasm) was increased in the *Ift20 KO* when compared to control mice (Figure S5I). We also found that the mutants showed an increase in the percentage of YAP1-AMOTL1 double-positive cells (Figure 3H). Together, these data show that the increased PE size in *Ift20 KO* mice is associated with increased YAP1 activity.

IFTs Interact with YAP1 and Regulate Its Activity

Taking advantage of cultured cells, we next explored the mechanism by which IFT proteins could regulate YAP1 activity. IF performed in HeLa cells transfected with IFT88-GFP showed colocalization between IFT88 and YAP1 in the cytoplasm (Figures S6A–S6C). To confirm a potential physical interaction between IFT proteins with YAP1, we performed co-immunoprecipitation (co-IP) experiments using IFT88-GFP and YAP1-Myc in HeLa cells but never obtained any clear interaction. Considering that YAP1 often necessitates the scaffold protein Angiomotin-like 1 (Amotl1) (Ragni et al., 2017), we next performed co-IP experiment using HA-Amotl1, IFT88-GFP, and YAP1-Myc in HeLa cells. The experiments revealed a clear interaction between YAP1, Amotl1, and IFT88 (Figure 4A). Similarly, physical interaction between endogenous YAP1, Flag-Amotl1, and IFT20-GFP was observed in transfected HEK293 cells (Figure 4A). These results reveal that IFT proteins, YAP1, and Amotl1 could function as part of a complex involved in the functional modulation of YAP1 activity *in vivo*.

To functionally assess the impact of endogenous IFT88 depletion on YAP1 activity, we used a DLD-1 IFT88-auxin-inducible degron (AID) cell line, in which a rapid degradation of IFT88 protein can be induced by auxin treatment (Figure 4B). Of note, DLD-1 cells do not grow cilia, allowing us to explore the cytoplasmic, cilia-independent function of IFT88 (Lancaster et al., 2011).

We observed that 2 h of auxin treatment led to IFT88 and YAP1 degradation. The rapid co-degradation further suggested that both proteins physically interact (Figure 4C). We confirmed this finding by performing shorter auxin treatments to study the progressive degradation of IFT88 and YAP1 (Figure 4C′). Importantly, as previously observed *in vivo*, longer depletion of endogenous IFT88 after 6 h of auxin treatment led to an increase in nuclear YAP1 measured by IF (Figure 4D). Consistently, the nuclear/cytoplasmic YAP1 ratio was also increased (Figure S7A). Additionally, we confirmed these results using HeLa and MDCK cell lines where IFT88 function was inactivated by IFT88-siRNA. The IFT88-siRNA efficiency was validated by IF

(E′) Immunofluorescence (IF) confocal images of MDCK cells treated with NT- or IFT88-siRNA (48 h). DAPI (blue) and YAP/WWTR1 (TAZ) (white inverted LUT). (F) Graph shows the increase in YAP/WWTR1 (TAZ) nuclear signal in IFT88-siRNA (48 h)-treated HeLa cells (n = 5 replicates, average cell number analyzed for each condition = 252; t test, p value, 0.02). Box and whiskers (5th–95th percentile). Outliers are represented as red dots (NT-siRNA) or blue squares (IFT88-siRNA). (F′) IF confocal images of HeLa cells treated with NT- or IFT88-siRNA (48 h). DAPI (blue) and YAP/WWTR1 (TAZ) (white inverted LUT).

and western blot (Figures S7E–S7G). After 48 h of IFT88-siRNA treatment, nuclear YAP1 signal was measured by IF (Figures 4E–4F′). The inactivation of IFT88 was accompanied with increased nuclear YAP1 (Figures 4E and 4F). Altogether, these data indicate that IFT88 can interact with YAP1 in the cytoplasm and is involved in modulating the activation of the Hippo pathway effector YAP1.

To confirm that increased nuclear YAP1 is specific of IFT protein function, we performed IFT88 and IFT20 overexpression assays. While the transfection of pEGFP C1 did not alter the nuclear signal between GFP-positive and GFP-negative cells (endogenous control) (Figure S6D), IFT88-GFP and IFT20-GFP overexpression caused a decrease in nuclear signal (Figures S7B–S7D). Together, these data confirm that IFT proteins modulate YAP1 activation.

DISCUSSION

IFT proteins have long been associated with ciliary functions in developmental processes. For example, *ift88* mutants display a number of phenotypes reminiscent of ciliary defects such as abnormal patterning of the neural tube, defects in the Hedgehog pathway and left-right patterning (Huang and Schier, 2009). Ift88 has also been associated with planar cell polarity (Cao et al., 2010) and cell division (Delaval et al., 2011; Taulet et al., 2017, 2019; Vitre et al., 2020). Our observations provide evidence for a role of IFT complex B proteins in cardiogenesis. Mechanistically, IFT proteins are best known for their function in ciliary transport (Ocbina et al., 2011). Here, we describe an unexpected interaction between the ciliary machinery proteins and a potent mechanosensing pathway, the Hippo pathway. The hippo effector YAP1 is known to have essential roles in cancer (Zanconato et al., 2016), regeneration (Bassat et al., 2017; Leach et al., 2017; Oh et al., 2018), and organ size control (Artap et al., 2018; Thompson and Sahai, 2015; Yu et al., 2015). Several mechanisms have been shown to regulate the shuttling of YAP1 into the nucleus, including phosphorylation by Hippo kinases. Recent studies show that YAP1 is mechanosensitive and that force applied to the nucleus can directly drive YAP1 nuclear translocation (Elosegui-Artola et al., 2017; Sun et al., 2014). Additionally, Angiomotin (AMOT) has been shown to interact physically with YAP1 and act as a buffering factor sequestering YAP1 in the cytoplasm (Zhao et al., 2011). Nevertheless, AMOTL1 has also been shown to co-localize with YAP1 in the nucleus (Ragni et al., 2017; Yi et al., 2013), demonstrating that YAP1 subcellular localization is highly regulated by Motin family proteins. Our results indicate that IFT complex B proteins are also involved in regulating YAP1 localization. We demonstrate that IFT88 interacts biochemically with YAP1 and both co-localize in the cytoplasm. We did not study TAZ, the other Hippo effector that is known to act with YAP1 (Piccolo et al., 2014), and we cannot draw general conclusions on the role of IFT88 on all the known Hippo effectors. Nevertheless, our work suggests alternative ways to interpret Ift88 mutant phenotypes, which are often interpreted based on polarity or cilia function issues, and, more generally, phenotypes of other mutants with abnormal IFT complex B proteins. Our working model is that Ift88 participates in sequestering YAP1 away from the nucleus using its cargo transport activity. Other cilia-related proteins, such as kinesin2 and IFT complex A proteins, have been shown to promote nuclear localization of β-catenin during Wnt signaling in *Drosophila* (Vuong et al., 2018), further suggesting that proteins identified for their ciliary transport functions are not always limited to that function. Future work will reveal the mechanism by which Ift88 limits nuclear translocation of YAP1 and address whether IFT complex A proteins play a role.

Importantly, while our study points toward a noncanonical function for IFT complex B proteins, our results do not exclude a role for primary cilia in PE formation. We found that *iguana/dzip* mutants display an avcPE phenotype, suggesting that primary cilia function is required for PE morphogenesis. The HH pathway is often associated with ciliary function. To date, a number of studies suggest the proepicardium and epicardium formation are not regulated by Hedgehog signaling (Rudat et al., 2013; Sugimoto et al., 2017). Indeed, dissection of zebrafish *shha* function in the PE and epicardium using a *tcf21:CreER*, a well-established PE and epicardial tissue driver (Robb et al., 1998), does not affect PE formation (Sugimoto et al., 2017). Besides, expression of *Shh*, *Dhh*, *Ihh*, and *Ptch1* was neither detected in the mouse PE nor in the epicardium at subsequent stages (Rudat et al., 2013). Thus, primary cilia certainly operate independently of the HH pathway and Yap1, which is not altered in *dzip* mutants, in the process. Our work further highlights the important role of the BMP pathway in PE formation (Andrés-Delgado et al., 2019; Liu and Stainier, 2010). Primary cilia modulate BMP pathway and, more generally, TGF beta signaling pathways (Mönnich et al., 2018; Villalobos et al., 2019). In endothelial cells, primary cilia modulate angiogenesis by altering BMP signaling (Vion et al., 2018). We speculate the situation is different in PE cells, where BMP is activated downstream of YAP1, and where IFT88 helps to limit YAP1 and BMP signaling. Similarly, Hippo signaling determines the number of atrial myocardial cells that originate from the SHF by modulating BMP signaling (Fukui et al., 2018). Interestingly, lack of Ift88 did not affect Isl1 expression at early stages, suggesting Ift88 modulates Yap1-BMP axis at later stages during PE and atrial myocardium development. While *yap1* zebrafish mutants display decreased myocardial cell number, they surprisingly display normal avcPE cell number. The zebrafish *yap1* mutants are able to develop and to reach adulthood, which can be due to the compensation between Yap1 and Wwtr1 previously described (Miesfeld et al., 2015). We speculate that similar compensation may be at work in the PE as well. Importantly, we found phenotypic difference between mouse and fish, especially regarding the heart size, which is not affected in mouse. More work will be needed to understand these interspecific differences as well as the potential mechanisms of compensation involved if any. Zebrafish, *ift88* and *elipsa*, and mouse, *Ift20* and *Ift88*, mutants are lethal at 6 dpf and E10.5–E11.5, respectively, making impossible the study of cardiovascular defects at later stages without conditional gene inactivation approaches.

In summary, our study reports the role of IFT complex B proteins during PE development by modulating YAP1 activity independently of any cilia function. Linking IFT with YAP1 activity might have important implications for understanding the etiology of ciliopathies during cardiogenesis and for the interpretation of ciliary defects in IFT mutants.

STAR★METHODS

Detailed methods are provided in the online version of this paper and include the following:

- KEY RESOURCES TABLE
- RESOURCE AVAILABILITY
  - Lead Contact
  - Materials Availability
  - Data and Code Availability
- EXPERIMENTAL MODEL AND SUBJECT DETAILS
  - Zebrafish (ZF) Models
  - Mouse Models
- METHOD DETAILS
  - *In Vivo* Imaging
  - ZF Treatments
  - ZF Immunofluorescence
  - *In Situ* Hybridization (ISH)
  - Whole Mount Immunofluorescence in the Mouse
  - Immunofluorescence on Cryosections in the Mouse
  - Cell Culture, siRNAs and Transfection
  - Generation of DLD-1 IFT88-AID Targeted Cells
  - Immunofluorescence on Cells
  - Lysates and Immunoblotting
- IMMUNOPRECIPITATION (IP) ASSAYS
  - HEK293 Cells
  - HeLa Cells
  - ZF avcPE Cell Quantification
  - ZF Myocardial Cell Quantification
  - Mice PE Volume Analysis
  - Mice Yap1- and Amotl1-Positive Cell Quantifications
  - Nuclear Yap Quantifications on Cells
  - Nuclear/cytoplasmic Yap1 Ratio
- QUANTIFICATION AND STATISTICAL ANALYSIS

SUPPLEMENTAL INFORMATION

Supplemental Information can be found online at https://doi.org/10.1016/j.celrep.2020.107932.

ACKNOWLEDGMENTS

We thank P. Lamperti, E. Steed, A. Bhat, D. Riveline, S. Harlepp, J. Godin, A. Benmerah, and the Vermot laboratory for discussion and thoughtful comments on the manuscript, in particular R. Chow for her help with editing. We thank S. Roth for technical help. We thank G. Pazour, M. Faucourt, and N. Spassky for advice, for the gift of plasmids, and for providing the *Ift20* and *Ift88* mutant mouse lines, and C. Cimper, L. Bombardelli, and C. Shea for technical assistance. We are grateful to the IGBMC fish facility, the IGBMC imaging center, and the imaging platforms of the SFR Necker. This project has received funding from the European Union's Horizon 2020 Research and Innovation Programme under the Marie Sklodowska-Curie Grant Agreement No. 708312 (M.P.) and from the European Research Council (ERC) under the European Union's Horizon 2020 Research and Innovation Programme: GA No. 682938 (J.V.). This work was supported by FRM (DEQ20140329553), by ANR (ANR-15-CE13-0015–liveheart, ANR- SNF310030E-164245-forcinregeneration), and by the Grant ANR-10-LABX-0030-INRT, a French State fund managed by the Agence Nationale de la Recherche under the frame program Investissements d'Avenir labeled ANR-10-IDEX-0002-02. B.D.'s team was supported by ANR-12-CHEX-005 and CNRS. S.M.M.'s team was supported by core funding from the Institut Imagine, Institut Pasteur, Inserm, Université Paris Descartes, and a grant from the AFM-Téléthon (Trampoline 18727). T.L. was funded by the ED515 (1691/2014). L.O.L. is supported by the European Commission (H2020-MSCA-ITN-2016 European Industrial Doctorate 4DHeart 722427).

AUTHOR CONTRIBUTIONS

Conceptualization, M.P. and J.V.; Data Curation, M.P., L.O.L., K.J., and T.L.; Formal Analysis, M.P.; Funding Acquisition, M.P., B.D., S.M.M., and J.V.; Investigation, M.P., L.O.L., K.J., T.L., B.V., D.H., and L.G.; Methodology, M.P., K.J., T.L., B.V., B.D., S.M.M., and J.V.; Project Administration, M.P. and J.V.; Resources, C.D., V.L., I.S., B.D., S.M.M., and J.V.; Supervision, J.V.; Validation, M.P., B.D., S.M.M., and J.V.; Visualization, M.P.; Writing – Original Draft, M.P. and J.V.; Writing – Review & Editing, M.P., L.O.L., K.J., T.L., D.H., C.D., B.V., N.M., V.L., B.D., S.M.M., and J.V.

DECLARATION OF INTERESTS

The authors declare no competing interests.

Received: October 24, 2019
Revised: April 30, 2020
Accepted: June 29, 2020
Published: July 21, 2020

REFERENCES

Acharya, A., Baek, S.T., Huang, G., Eskiocak, B., Goetsch, S., Sung, C.Y., Banfi, S., Sauer, M.F., Olsen, G.S., Duffield, J.S., et al. (2012). The bHLH transcription factor Tcf21 is required for lineage-specific EMT of cardiac fibroblast progenitors. Development *139*, 2139–2149.

Agarwala, S., Duquesne, S., Liu, K., Boehm, A., Grimm, L., Link, S., König, S., Eimer, S., Ronneberger, O., and Lecaudey, V. (2015). Amotl2a interacts with the Hippo effector Yap1 and the Wnt/β-catenin effector Lef1 to control tissue size in zebrafish. eLife *4*, e08201.

Andrés-Delgado, L., Ernst, A., Galardi-Castilla, M., Bazaga, D., Peralta, M., Münch, J., González-Rosa, J.M., Marques, I., Tessadori, F., de la Pompa, J.L., et al. (2019). Actin dynamics and the Bmp pathway drive apical extrusion of proepicardial cells. Development *146*, dev174961.

Artap, S., Manderfield, L.J., Smith, C.L., Poleshko, A., Aghajanian, H., See, K., Li, L., Jain, R., and Epstein, J.A. (2018). Endocardial Hippo signaling regulates myocardial growth and cardiogenesis. Dev. Biol. *440*, 22–30.

Bassat, E., Mutlak, Y.E., Genzelinakh, A., Shadrin, I.Y., Baruch Umansky, K., Yifa, O., Kain, D., Rajchman, D., Leach, J., Riabov Bassat, D., et al. (2017). The extracellular matrix protein agrin promotes heart regeneration in mice. Nature *547*, 179–184.

Berbari, N.F., O'Connor, A.K., Haycraft, C.J., and Yoder, B.K. (2009). The primary cilium as a complex signaling center. Curr. Biol. *19*, R526–R535.

Boin, A., Couvelard, A., Couderc, C., Brito, I., Filipescu, D., Kalamarides, M., Bedossa, P., De Koning, L., Danelsky, C., Dubois, T., et al. (2014). Proteomic screening identifies a YAP-driven signaling network linked to tumor cell proliferation in human schwannomas. Neuro-oncol. *16*, 1196–1209.

Borovina, A., Superina, S., Voskas, D., and Ciruna, B. (2010). Vangl2 directs the posterior tilting and asymmetric localization of motile primary cilia. Nat. Cell Biol. *12*, 407–412.

Bratt, A., Wilson, W.J., Troyanovsky, B., Aase, K., Kessler, R., Van Meir, E.G., and Holmgren, L. (2002). Angiomotin belongs to a novel protein family with conserved coiled-coil and PDZ binding domains. Gene *298*, 69–77.

Buckingham, M., Meilhac, S., and Zaffran, S. (2005). Building the mammalian heart from two sources of myocardial cells. Nat. Rev. Genet. *6*, 826–835.

Cao, Y., Park, A., and Sun, Z. (2010). Intraflagellar transport proteins are essential for cilia formation and for planar cell polarity. J. Am. Soc. Nephrol. *21*, 1326–1333.

Carmona, R., González-Iriarte, M., Pérez-Pomares, J.M., and Muñoz-Chápuli, R. (2001). Localization of the Wilm's tumour protein WT1 in avian embryos. Cell Tissue Res. *303*, 173–186.

Cong, L., Ran, F.A., Cox, D., Lin, S., Barretto, R., Habib, N., Hsu, P.D., Wu, X., Jiang, W., Marraffini, L.A., and Zhang, F. (2013). Multiplex genome engineering using CRISPR/Cas systems. Science *339*, 819–823.

de Pater, E., Clijsters, L., Marques, S.R., Lin, Y.F., Garavito-Aguilar, Z.V., Yelon, D., and Bakkers, J. (2009). Distinct phases of cardiomyocyte differentiation regulate growth of the zebrafish heart. Development *136*, 1633–1641.

Delaval, B., Bright, A., Lawson, N.D., and Doxsey, S. (2011). The cilia protein IFT88 is required for spindle orientation in mitosis. Nat. Cell Biol. *13*, 461–468.

DeRan, M., Yang, J., Shen, C.-H., Peters, E.C., Fitamant, J., Chan, P., Hsieh, M., Zhu, S., Asara, J.M., Zheng, B., et al. (2014). Energy stress regulates hippo-YAP signaling involving AMPK-mediated regulation of angiomotin-like 1 protein. Cell Rep. *9*, 495–503.

Elosegui-Artola, A., Andreu, I., Beedle, A.E.M., Lezamiz, A., Uroz, M., Kosmalska, A.J., Oria, R., Kechagia, J.Z., Rico-Lastres, P., Le Roux, A.-L., et al. (2017). Force triggers YAP nuclear entry by regulating transport across nuclear pores. Cell *171*, 1397–1410.e14.

Ferreira, RR, Fukui, H, Chow, R, Vilfan, A, Vermot, J (Eds.), 2019 Jul. The cilium as a force sensor-myth versus reality. J Cell Sci 30132, jcs213496.

Finetti, F., Paccani, S.R., Riparbelli, M.G., Giacomello, E., Perinetti, G., Pazour, G.J., Rosenbaum, J.L., and Baldari, C.T. (2009). Intraflagellar transport is required for polarized recycling of the TCR/CD3 complex to the immune synapse. Nat. Cell Biol. *11*, 1332–1339.

Follit, J.A., Tuft, R.A., Fogarty, K.E., and Pazour, G.J. (2006). The intraflagellar transport protein IFT20 is associated with the Golgi complex and is required for cilia assembly. Mol. Biol. Cell *17*, 3781–3792.

Frank, V., Habbig, S., Bartram, M.P., Eisenberger, T., Veenstra-Knol, H.E., Decker, C., Boorsma, R.A.C., Göbel, H., Nürnberg, G., Griessmann, A., et al. (2013). Mutations in NEK8 link multiple organ dysplasia with altered Hippo signalling and increased c-MYC expression. Hum. Mol. Genet. *22*, 2177–2185.

Fukui, H., Miyazaki, T., Chow, R.W.-Y., Ishikawa, H., Nakajima, H., Vermot, J., and Mochizuki, N. (2018). Hippo signaling determines the number of venous pole cells that originate from the anterior lateral plate mesoderm in zebrafish. eLife *7*, e29106.

Galgano, D., Onnis, A., Pappalardo, E., Galvagni, F., Acuto, O., and Baldari, C.T. (2017). The T cell IFT20 interactome reveals new players in immune synapse assembly. J. Cell Sci. *130*, 1110–1121.

González-Rosa, J.M., Peralta, M., and Mercader, N. (2012). Pan-epicardial lineage tracing reveals that epicardium derived cells give rise to myofibroblasts and perivascular cells during zebrafish heart regeneration. Dev. Biol. *370*, 173–186.

Grampa, V., Delous, M., Zaidan, M., Odye, G., Thomas, S., Elkhartoufi, N., Filhol, E., Niel, O., Silbermann, F., Lebreton, C., et al. (2016). Novel NEK8 mutations cause severe syndromic renal cystic dysplasia through YAP dysregulation. PLoS Genet. *12*, e1005894.

Habbig, S., Bartram, M.P., Sägmüller, J.G., Griessmann, A., Franke, M., Müller, R.-U., Schwarz, R., Hoehne, M., Bergmann, C., Tessmer, C., et al. (2012). The ciliopathy disease protein NPHP9 promotes nuclear delivery and activation of the oncogenic transcriptional regulator TAZ. Hum. Mol. Genet. *21*, 5528–5538.

Haycraft, C.J., Zhang, Q., Song, B., Jackson, W.S., Detloff, P.J., Serra, R., and Yoder, B.K. (2007). Intraflagellar transport is essential for endochondral bone formation. Development *134*, 307–316.

He, M., Subramanian, R., Bangs, F., Omelchenko, T., Liem, K.F., Jr., Kapoor, T.M., and Anderson, K.V. (2014). The kinesin-4 protein Kif7 regulates mammalian Hedgehog signalling by organizing the cilium tip compartment. Nat. Cell Biol. *16*, 663–672.

Holland, A.J., Fachinetti, D., Han, J.S., and Cleveland, D.W. (2012). Inducible, reversible system for the rapid and complete degradation of proteins in mammalian cells. Proc. Natl. Acad. Sci. USA *109*, E3350–E3357.

Hua, K., and Ferland, R.J. (2018). Primary cilia proteins: ciliary and extraciliary sites and functions. Cell. Mol. Life Sci. *75*, 1521–1540.

Huang, P., and Schier, A.F. (2009). Dampened Hedgehog signaling but normal Wnt signaling in zebrafish without cilia. Development *136*, 3089–3098.

Ishii, Y., Garriock, R.J., Navetta, A.M., Coughlin, L.E., and Mikawa, T. (2010). BMP signals promote proepicardial protrusion necessary for recruitment of coronary vessel and epicardial progenitors to the heart. Dev. Cell *19*, 307–316.

Jonassen, J.A., San Agustin, J., Follit, J.A., and Pazour, G.J. (2008). Deletion of IFT20 in the mouse kidney causes misorientation of the mitotic spindle and cystic kidney disease. J. Cell Biol. *183*, 377–384.

Katz, T.C., Singh, M.K., Degenhardt, K., Rivera-Feliciano, J., Johnson, R.L., Epstein, J.A., and Tabin, C.J. (2012). Distinct compartments of the proepicardial organ give rise to coronary vascular endothelial cells. Dev. Cell *22*, 639–650.

Kikuchi, K., and Poss, K.D. (2012). Cardiac regenerative capacity and mechanisms. Annu. Rev. Cell Dev. Biol. *28*, 719–741.

Kikuchi, K., Gupta, V., Wang, J., Holdway, J.E., Wills, A.A., Fang, Y., and Poss, K.D. (2011). tcf21^{+} epicardial cells adopt non-myocardial fates during zebrafish heart development and regeneration. Development *138*, 2895–2902.

Kim, H.R., Richardson, J., van Eeden, F., and Ingham, P.W. (2010). Gli2a protein localization reveals a role for Iguana/DZIP1 in primary ciliogenesis and a dependence of Hedgehog signal transduction on primary cilia in the zebrafish. BMC Biol. *8*, 65.

Kim, M., Kim, M., Lee, M.-S., Kim, C.-H., and Lim, D.-S. (2014). The MST1/2-SAV1 complex of the Hippo pathway promotes ciliogenesis. Nat. Commun. *5*, 5370.

Klena, N., Gabriel, G., Liu, X., Yagi, H., Li, Y., Chen, Y., Zahid, M., Tobita, K., Leatherbury, L., Pazour, G., and Lo, C.W. (2016). Role of cilia and left-right patterning in congenital heart disease. Etiology and Morphogenesis of Congenital Heart Disease: From Gene Function and Cellular Interaction to Morphology (Springer), p. 1.

Lai, J.K.H., Collins, M.M., Uribe, V., Jiménez-Amilburu, V., Günther, S., Maischein, H.-M., and Stainier, D.Y.R. (2018). The Hippo pathway effector Wwtr1 regulates cardiac wall maturation in zebrafish. Development *145*, dev159210.

Lallemand, Y., Luria, V., Haffner-Krausz, R., and Lonai, P. (1998). Maternally expressed PGK-Cre transgene as a tool for early and uniform activation of the Cre site-specific recombinase. Transgenic Res. *7*, 105–112.

Lancaster, M.A., Schroth, J., and Gleeson, J.G. (2011). Subcellular spatial regulation of canonical Wnt signalling at the primary cilium. Nat. Cell Biol. *13*, 700–707.

Leach, J.P., Heallen, T., Zhang, M., Rahmani, M., Morikawa, Y., Hill, M.C., Segura, A., Willerson, J.T., and Martin, J.F. (2017). Hippo pathway deficiency reverses systolic heart failure after infarction. Nature *550*, 260–264.

Li, Y., Klena, N.T., Gabriel, G.C., Liu, X., Kim, A.J., Lemke, K., Chen, Y., Chatterjee, B., Devine, W., Damerla, R.R., et al. (2015). Global genetic analysis in mice unveils central role for cilia in congenital heart disease. Nature *521*, 520–524.

Limana, F., Capogrossi, M.C., and Germani, A. (2011). The epicardium in cardiac repair: from the stem cell view. Pharmacol. Ther. *129*, 82–96.

Liu, J., and Stainier, D.Y.R. (2010). Tbx5 and Bmp signaling are essential for proepicardium specification in zebrafish. Circ. Res. *106*, 1818–1828.

Liu-Chittenden, Y., Huang, B., Shim, J.S., Chen, Q., Lee, S.-J., Anders, R.A., Liu, J.O., and Pan, D. (2012). Genetic and pharmacological disruption of the TEAD-YAP complex suppresses the oncogenic activity of YAP. Genes Dev. *26*, 1300–1305.

Männer, J., Schlueter, J., and Brand, T. (2005). Experimental analyses of the function of the proepicardium using a new microsurgical procedure to induce loss-of-proepicardial-function in chick embryos. Dev. Dyn. *233*, 1454–1463.

Miesfeld, J.B., and Link, B.A. (2014). Establishment of transgenic lines to monitor and manipulate Yap/Taz-Tead activity in zebrafish reveals both evolutionarily conserved and divergent functions of the Hippo pathway. Mech. Dev. *133*, 177–188.

Miesfeld, J.B., Gestri, G., Clark, B.S., Flinn, M.A., Poole, R.J., Bader, J.R., Besharse, J.C., Wilson, S.W., and Link, B.A. (2015). Yap and Taz regulate retinal pigment epithelial cell fate. Development *142*, 3021–3032.

Mikawa, T., and Fischman, D.A. (1992). Retroviral analysis of cardiac morphogenesis: discontinuous formation of coronary vessels. Proc. Natl. Acad. Sci. USA *89*, 9504–9508.

Mikawa, T., and Gourdie, R.G. (1996). Pericardial mesoderm generates a population of coronary smooth muscle cells migrating into the heart along with ingrowth of the epicardial organ. Dev. Biol. *174*, 221–232.

Mommersteeg, M.T.M., Domínguez, J.N., Wiese, C., Norden, J., de Gier-de Vries, C., Burch, J.B.E., Kispert, A., Brown, N.A., Moorman, A.F.M., and Christoffels, V.M. (2010). The sinus venosus progenitors separate and diversify from the first and second heart fields early in development. Cardiovasc. Res. *87*, 92–101.

Mönnich, M., Borgeskov, L., Breslin, L., Jakobsen, L., Rogowski, M., Doganli, C., Schrøder, J.M., Mogensen, J.B., Blinkenkjær, L., Harder, L.M., et al. (2018). CEP128 localizes to the subdistal appendages of the mother centriole and regulates TGF-β/BMP signaling at the primary cilium. Cell Rep. *22*, 2584–2592.

Moore, A.W., McInnes, L., Kreidberg, J., Hastie, N.D., and Schedl, A. (1999). YAC complementation shows a requirement for Wt1 in the development of epicardium, adrenal gland and throughout nephrogenesis. Development *126*, 1845–1857.

Nakajima, H., Yamamoto, K., Agarwala, S., Terai, K., Fukui, H., Fukuhara, S., Ando, K., Miyazaki, T., Yokota, Y., Schmelzer, E., et al. (2017). Flow-dependent endothelial YAP regulation contributes to vessel maintenance. Dev. Cell *40*, 523–536.e6.

Ocbina, P.J.R., Eggenschwiler, J.T., Moskowitz, I., and Anderson, K.V. (2011). Complex interactions between genes controlling trafficking in primary cilia. Nat. Genet. *43*, 547–553.

Oh, S.-H., Swiderska-Syn, M., Jewell, M.L., Premont, R.T., and Diehl, A.M. (2018). Liver regeneration requires Yap1-TGFβ-dependent epithelial-mesenchymal transition in hepatocytes. J. Hepatol. *69*, 359–367.

Omori, Y., Zhao, C., Saras, A., Mukhopadhyay, S., Kim, W., Furukawa, T., Sengupta, P., Veraksa, A., and Malicki, J. (2008). Elipsa is an early determinant of ciliogenesis that links the IFT particle to membrane-associated small GTPase Rab8. Nat. Cell Biol. *10*, 437–444.

Pazour, G.J., Dickert, B.L., Vucica, Y., Seeley, E.S., Rosenbaum, J.L., Witman, G.B., and Cole, D.G. (2000). *Chlamydomonas IFT88* and its mouse homologue, polycystic kidney disease gene tg737, are required for assembly of cilia and flagella. J. Cell Biol. *151*, 709–718.

Pei, Z., Bai, Y., and Schmitt, A.P. (2010). PIV5 M protein interaction with host protein angiomotin-like 1. Virology *397*, 155–166.

Peralta, M., Steed, E., Harlepp, S., González-Rosa, J.M., Monduc, F., Ariza-Cosano, A., Cortés, A., Rayón, T., Gómez-Skarmeta, J.-L., Zapata, A., et al. (2013). Heartbeat-driven pericardiac fluid forces contribute to epicardium morphogenesis. Curr. Biol. *23*, 1726–1735.

Piccolo, S., Dupont, S., and Cordenonsi, M. (2014). The biology of YAP/TAZ: hippo signaling and beyond. Physiol. Rev. *94*, 1287–1312.

Ragni, C.V., Diguet, N., Le Garrec, J.-F., Novotova, M., Resende, T.P., Pop, S., Charon, N., Guillemot, L., Kitasato, L., Badouel, C., et al. (2017). Amotl1 mediates sequestration of the Hippo effector Yap1 downstream of Fat4 to restrict heart growth. Nat. Commun. *8*, 14582.

Reiter, J.F., and Leroux, M.R. (2017). Genes and molecular pathways underpinning ciliopathies. Nat. Rev. Mol. Cell Biol. *18*, 533–547.

Robb, L., Mifsud, L., Hartley, L., Biben, C., Copeland, N.G., Gilbert, D.J., Jenkins, N.A., and Harvey, R.P. (1998). epicardin: a novel basic helix-loop-helix transcription factor gene expressed in epicardium, branchial arch myoblasts, and mesenchyme of developing lung, gut, kidney, and gonads. Dev. Dyn. *213*, 105–113.

Robert, A., Margall-Ducos, G., Guidotti, J.-E., Brégerie, O., Celati, C., Bréchot, C., and Desdouets, C. (2007). The intraflagellar transport component IFT88/polaris is a centrosomal protein regulating G1-S transition in non-ciliated cells. J. Cell Sci. *120*, 628–637.

Rosenbaum, J.L., and Witman, G.B. (2002). Intraflagellar transport. Nat. Rev. Mol. Cell Biol. *3*, 813–825.

Rudat, C., Norden, J., Taketo, M.M., and Kispert, A. (2013). Epicardial function of canonical Wnt-, Hedgehog-, Fgfr1/2-, and Pdgfra-signalling. Cardiovasc. Res. *100*, 411–421.

San Agustin, J.T., Klena, N., Granath, K., Panigrahy, A., Stewart, E., Devine, W., Strittmatter, L., Jonassen, J.A., Liu, X., Lo, C.W., and Pazour, G.J. (2016). Genetic link between renal birth defects and congenital heart disease. Nat. Commun. *7*, 11103.

Schindelin, J., Arganda-Carreras, I., Frise, E., Kaynig, V., Longair, M., Pietzsch, T., Preibisch, S., Rueden, C., Saalfeld, S., Schmid, B., et al. (2012). Fiji: an open-source platform for biological-image analysis. Nat. Methods *9*, 676–682.

Schlueter, J., Männer, J., and Brand, T. (2006). BMP is an important regulator of proepicardial identity in the chick embryo. Dev. Biol. *295*, 546–558.

Singh, A., Ramesh, S., Cibi, D.M., Yun, L.S., Li, J., Li, L., Manderfield, L.J., Olson, E.N., Epstein, J.A., and Singh, M.K. (2016). Hippo signaling mediators Yap and Taz are required in the epicardium for coronary vasculature development. Cell Rep. *15*, 1384–1393.

Slough, J., Cooney, L., and Brueckner, M. (2008). Monocilia in the embryonic mouse heart suggest a direct role for cilia in cardiac morphogenesis. Dev. Dyn. *237*, 2304–2314.

Sugimoto, K., Hui, S.P., Sheng, D.Z., and Kikuchi, K. (2017). Dissection of zebrafish *shha* function using site-specific targeting with a Cre-dependent genetic switch. eLife *6*, e24635.

Sun, Z., Amsterdam, A., Pazour, G.J., Cole, D.G., Miller, M.S., and Hopkins, N. (2004). A genetic screen in zebrafish identifies cilia genes as a principal cause of cystic kidney. Development *131*, 4085–4093.

Sun, Y., Yong, K.M.A., Villa-Diaz, L.G., Zhang, X., Chen, W., Philson, R., Weng, S., Xu, H., Krebsbach, P.H., and Fu, J. (2014). Hippo/YAP-mediated rigidity-dependent motor neuron differentiation of human pluripotent stem cells. Nat. Mater. *13*, 599–604.

Taschner, M., Bhogaraju, S., and Lorentzen, E. (2012). Architecture and function of IFT complex proteins in ciliogenesis. Differentiation *83*, S12–S22.

Taulet, N., Vitre, B., Anguille, C., Douanier, A., Rocancourt, M., Taschner, M., Lorentzen, E., Echard, A., and Delaval, B. (2017). IFT proteins spatially control the geometry of cleavage furrow ingression and lumen positioning. Nat. Commun. *8*, 1928.

Taulet, N., Douanier, A., Vitre, B., Anguille, C., Maurin, J., Dromard, Y., Georget, V., and Delaval, B. (2019). IFT88 controls NuMA enrichment at k-fibers minus-ends to facilitate their re-anchoring into mitotic spindles. Sci. Rep. *9*, 10311.

Tay, S.Y., Yu, X., Wong, K.N., Panse, P., Ng, C.P., and Roy, S. (2010). The iguana/DZIP1 protein is a novel component of the ciliogenic pathway essential for axonemal biogenesis. Dev. Dyn. *239*, 527–534.

Thisse, C., and Thisse, B. (2008). High-resolution *in situ* hybridization to whole-mount zebrafish embryos. Nat Protoc *3*, 59–69.

Thompson, B.J., and Sahai, E. (2015). MST kinases in development and disease. J. Cell Biol. *210*, 871–882.

Tsujikawa, M., and Malicki, J. (2004). Intraflagellar transport genes are essential for differentiation and survival of vertebrate sensory neurons. Neuron *42*, 703–716.

van Wijk, B., van den Berg, G., Abu-Issa, R., Barnett, P., van der Velden, S., Schmidt, M., Ruijter, J.M., Kirby, M.L., Moorman, A.F.M., and van den Hoff, M.J.B. (2009). Epicardium and myocardium separate from a common precursor pool by crosstalk between bone morphogenetic protein- and fibroblast growth factor-signaling pathways. Circ. Res. *105*, 431–441.

Vertii, A., Bright, A., Delaval, B., Hehnly, H., and Doxsey, S. (2015). New frontiers: discovering cilia-independent functions of cilia proteins. EMBO Rep. *16*, 1275–1287.

Villalobos, E., Criollo, A., Schiattarella, G.G., Altamirano, F., French, K.M., May, H.I., Jiang, N., Nguyen, N.U.N., Romero, D., Roa, J.C., et al. (2019). Fibroblast primary cilia are required for cardiac fibrosis. Circulation *139*, 2342–2357.

Vion, A.-C., Alt, S., Klaus-Bergmann, A., Szymborska, A., Zheng, T., Perovic, T., Hammoutene, A., Oliveira, M.B., Bartels-Klein, E., Hollfinger, I., et al. (2018). Primary cilia sensitize endothelial cells to BMP and prevent excessive vascular regression. J. Cell Biol. *217*, 1651–1665.

Vitre, B., Taulet, N., Guesdon, A., Douanier, A., Dosdane, A., Cisneros, M., Maurin, J., Hettinger, S., Anguille, C., Taschner, M., et al. (2020). IFT proteins interact with HSET to promote supernumerary centrosome clustering in mitosis. EMBO Rep. *21*, e49234.

Vuong, L.T., Iomini, C., Balmer, S., Esposito, D., Aaronson, S.A., and Mlodzik, M. (2018). Kinesin-2 and IFT-A act as a complex promoting nuclear localization of β-catenin during Wnt signalling. Nat. Commun. *9*, 5304.

Wang, W., Huang, J., and Chen, J. (2011). Angiomotin-like proteins associate with and negatively regulate YAP1. J. Biol. Chem. *286*, 4364–4370.

Wang, W., Li, N., Li, X., Tran, M.K., Han, X., and Chen, J. (2015). Tankyrase inhibitors target YAP by stabilizing angiomotin family proteins. Cell Rep. *13*, 524–532.

Witzel, H.R., Jungblut, B., Choe, C.P., Crump, J.G., Braun, T., and Dobreva, G. (2012). The LIM protein Ajuba restricts the second heart field progenitor pool by regulating Isl1 activity. Dev. Cell *23*, 58–70.

Wu, S.-P., Dong, X.-R., Regan, J.N., Su, C., and Majesky, M.W. (2013). Tbx18 regulates development of the epicardium and coronary vessels. Dev. Biol. *383*, 307–320.

Xin, M., Kim, Y., Sutherland, L.B., Qi, X., McAnally, J., Schwartz, R.J., Richardson, J.A., Bassel-Duby, R., and Olson, E.N. (2011). Regulation of insulin-like growth factor signaling by Yap governs cardiomyocyte proliferation and embryonic heart size. Sci. Signal. *4*, ra70.

Yi, C., Shen, Z., Stemmer-Rachamimov, A., Dawany, N., Troutman, S., Showe, L.C., Liu, Q., Shimono, A., Sudol, M., Holmgren, L., et al. (2013). The p130 isoform of angiomotin is required for Yap-mediated hepatic epithelial cell proliferation and tumorigenesis. Sci. Signal. *6*, ra77.

Yu, F.-X., Zhao, B., and Guan, K.-L. (2015). Hippo pathway in organ size control, tissue homeostasis, and cancer. Cell *163*, 811–828.

Zanconato, F., Cordenonsi, M., and Piccolo, S. (2016). YAP/TAZ at the roots of cancer. Cancer Cell *29*, 783–803.

Zhao, B., Ye, X., Yu, J., Li, L., Li, W., Li, S., Yu, J., Lin, J.D., Wang, C.Y., Chinnaiyan, A.M., et al. (2008). TEAD mediates YAP-dependent gene induction and growth control. Genes Dev. *22*, 1962–1971.

Zhao, B., Li, L., Lu, Q., Wang, L.H., Liu, C.-Y., Lei, Q., and Guan, K.-L. (2011). Angiomotin is a novel Hippo pathway component that inhibits YAP oncoprotein. Genes Dev. *25*, 51–63.

Zheng, Y., Vertuani, S., Nyström, S., Audebert, S., Meijer, I., Tegnebratt, T., Borg, J.-P., Uhlén, P., Majumdar, A., and Holmgren, L. (2009). Angiomotin-like protein 1 controls endothelial polarity and junction stability during sprouting angiogenesis. Circ. Res. *105*, 260–270.

Zhu, X., Liang, Y., Gao, F., and Pan, J. (2017). IFT54 regulates IFT20 stability but is not essential for tubulin transport during ciliogenesis. Cell. Mol. Life Sci. *74*, 3425–3437.

STAR★METHODS

KEY RESOURCES TABLE

REAGENT or RESOURCE	SOURCE	IDENTIFIER
Antibodies		
anti-myosin heavy chain	DSHB	Cat. # MF20; RRID:AB_2147781
anti-GFP	AVES	Cat. # GFP 1020; RRID:AB_10000240
anti-phospho-Smad 1/5 (Ser463/465)	Cell signaling	Cat. # 9516S; RRID:AB_491015
anti-phospho- Smad1/5/9	Cell signaling	Cat. #13820; RRID:AB_2493181
anti-Tbx18	Santa Cruz	Cat. # sc-17869; RRID:AB_2200374
anti-Yap1	Santa Cruz	Cat. # sc-101199; RRID:AB_1131430
anti-Yap1	Lecaudey laboratory	N/A
anti-Wt1	Santa Cruz	Cat. # sc-192; RRID:AB_632611
anti- Amotl1	Sigma	Cat. # HPA001196; RRID:AB_1078147
anti-γ-tubulin	Santa Cruz	Cat. # sc-17787; RRID:AB_628417
anti-α-tubulin	Sigma	Cat. # T6199; RRID:AB_477583
anti-IFT88	Euromedex	Cat. # 13967-1-AP; RRID:AB_2121979
anti-Islet1	Genetex	Cat. # GTX128201; RRID:AB_11179180
anti-Yap1	Cell signaling	Cat. # 4912; RRID:AB_2218911
anti-Yap/Taz	Cell signaling	Cat. # D24E4; RRID:AB_2799044
goat anti-chicken Alexa Fluor 488 IgY (H+L)	Invitrogen	Cat. # A-11039; RRID:AB_142924
goat anti-mouse IgG Cy3 conjugate (H+L)	Life technologies	Cat. # M30010; RRID:AB_2536619
goat anti-rabbit Alexa Fluor 647	ThermoFisher	Cat. # A-21244; RRID:AB_2535812
4′,6-diamidino-2-phenylindole (DAPI)	Invitrogen	Cat. # D1306; RRID:AB_2629482
anti-GFP	ThermoFisher	Cat. # CAB421; RRID AB_10709851
anti-FLAG	Sigma	Cat. # F7425; RRID:AB_439687
anti-Ift20	Proteintech	Cat. # 13615-1-AP; RRID:AB_2280001
anti-GFP	Abcam	Cat. # ab290; RRID:AB_303395
anti-HA	Roche	Cat. # 11867423001; RRID:AB_390918
Chemicals, Peptides, and Recombinant Proteins		
1-phenyl-2-thiourea (PTU)	Sigma-Aldrich	Cat. # P7629
Tricaine/MS-222	Sigma-Aldrich	Cat. # A-5040
UltraPure™ Low Melting Point Agarose	Invitrogen	Cat. # 16520-050
Verteporfin	Sigma-Aldrich	Cat. # SML0534
XAV939	Tocris Bioscience	Cat. # 3748
Phosphate buffered saline (PBS)	Sigma-Aldrich	Cat. # P4417
Indole-3-acetic acid sodium salt (Heteroauxin)	Sigma-Aldrich	Cat. # I5148
Lipofectamine® 2000 Transfection Reagent	ThermoFisher SCIENTIFIC	Cat. # 11668030
cOmpleteTM Protease Inhibitor Cocktail	Roche	Cat. # 11697498001
Opti-MEM	GIBCO	Cat. # 51985-026
Oligofectamine	Invitrogen	Cat. # 12252-01
Hoechst	ThermoFisher	Cat. # 62249
Experimental Models: Cell Lines		
HEK293 cells	Q-BIOgene	AES0503
MDCK cells	Sumara laboratory	N/A
HeLa cells	Sumara laboratory	N/A
DLD-1 IFT88-AID	Vitre et al., 2020	N/A

(*Continued on next page*)

Continued

REAGENT or RESOURCE	SOURCE	IDENTIFIER
Experimental Models: Organisms/Strains		
Zebrafish: *Et(−26.5Hsa.WT1-1gata2:EGFP)^{cn1}* (*epi:GFP*)	Peralta et al., 2013	ZFIN ID: ZDB-ALT-170823-7
Zebrafish: *iguana^{ts294e}*	Tay et al., 2010	ZFIN ID: ZDB-FISH-150901-16040
Zebrafish: *ift88 $^{tz288/oval}$*	Tsujikawa and Malicki, 2004	ZFIN ID: ZDB-ALT-980413-526
Zebrafish: *elipsa ^{tp49d}*	Omori et al., 2008	ZFIN ID: ZDB-ALT-980413-466
Zebrafish: *yap1 ^{fu48}*	Agarwala et al., 2015	ZFIN ID: ZDB-ALT-160413-4
Zebrafish: *amotl2a ^{fu46}*	Agarwala et al., 2015	ZFIN ID: ZDB-ALT-160412-2
Zebrafish: *4xGTIIC:d2GFP*	Miesfeld and Link, 2014	ZFIN ID: ZDB-ALT-150928-6
Zebrafish: *actb2:Mmu.Arl13b-GFP*	Borovina et al., 2010	ZFIN ID: ZDB-ALT-100721-1
Zebrafish: *tcf21:NLS-EGFP*	Kikuchi et al., 2011	ZFIN ID: ZDB-ALT-110914-2
Mice: *Ift20$^{null/+}$* (*C57BL* background)	Jonassen et al., 2008	MGI: 12565
Mice: PGK-Cre	Lallemand et al., 1998	PMID: 9608738
Mice: *Ift88$^{null/+}$* (*6JRj* background)	Haycraft et al., 2007	MGI:5505911
Oligonucleotides		
siRNA ON-Target plus - Control pool Non-targeting	Dharmacon	D-001810-10-05
siRNA ON-Target plus - SMART pool human IFT88	Dharmacon	L-012281-01
Recombinant DNA		
Flag-Amotl1	Pei et al., 2010	N/A
Ift20-GFP	Follit et al., 2006	N/A
YAP1-Myc	Boin et al., 2014	N/A
pEGFP-C1	Ragni et al., 2017	N/A
HA-Amotl1	Ragni et al., 2017	N/A
IFT88-GFP	He et al., 2014	N/A
Software and Algorithms		
FIJI	Schindelin et al., 2012	RRID:SCR_002285
Imaris	Bitplane	RRID: SCR_007370
MATLAB	MathWorks	RRID: SCR_001622
Microsoft Excel	Microsoft	RRID: SCR_016137
GraphPad Prism 7	GraphPad Software	RRID: SCR_002798
Other		
GFP-Trap	ChromoTek	Cat. # gta-10
anti-FLAG M2 Affinity gel	Sigma	Cat. # A2220

RESOURCE AVAILABILITY

Lead Contact

Further information and requests for reagents may be directed to and will be fulfilled by the Lead Contact, Julien Vermot (jvermot@imperial.ac.uk).

Materials Availability

This study did not generate new unique reagents.

Data and Code Availability

This study did not generate any unique datasets or code.

EXPERIMENTAL MODEL AND SUBJECT DETAILS

Zebrafish (ZF) Models

Animal experiments were approved by the Animal Experimentation Committee of the Institutional Review Board of the IGBMC. ZF lines used in the study were *Et(−26.5Hsa.WT1-1gata2:EGFP)*^{cn1} transgenic line (referred to as *epi:GFP*) (Peralta et al., 2013), *amotl2a* ^{fu46} (Agarwala et al., 2015), *elipsa* ^{tp49d} (Omori et al., 2008), *ift88* $^{tz288/oval}$ (Tsujikawa and Malicki, 2004), *iguana* ^{ts294e} (Tay et al., 2010), *yap1* ^{fu48} (Agarwala et al., 2015), *4xGTIIC:d2GFP* (Miesfeld and Link, 2014), *actb2:Mmu.Arl13b-GFP* (Borovina et al., 2010) and *tcf21:NLS-EGFP* (Kikuchi et al., 2011). Male and female samples were mixed. All animals were incubated at 28.5°C for 24h before treatment with 1-phenyl-2-thiourea (PTU) (Sigma Aldrich) to prevent pigment formation.

Mouse Models

Ift20$^{flox/+}$ (Jonassen et al., 2008) were crossed to PGK-Cre mice (Lallemand et al., 1998) to generate *Ift20*$^{null/+}$ maintained on a C57BL/6JRj genetic background. *Ift88*$^{null/+}$ (Haycraft et al., 2007) mice were maintained on a B6D2 genetic background. Animal procedures were approved by the ethical committee of the Institut Pasteur and the French Ministry of Research. E9.5 embryos were isolated in 200ng/ml cold heparin, incubated in cold 250mM KCl and fixed in 4% paraformaldehyde in PBS inside a rotative oven at 37°C overnight to remove excess of blood. Male and female samples were mixed.

METHOD DETAILS

In Vivo Imaging

ZF embryos were staged, anaesthetized with 0.02% tricaine solution and mounted in 0.7% low melting-point agarose (Sigma Aldrich). Confocal imaging was performed on a Leica SP8 confocal microscope. Images were acquired bidirectionally with a low-magnification water immersion objective (Leica HCX IRAPO L, 25X, N.A. 0.95). For time lapse, z stacks were acquired each 15 or 30 min, depending on the experiment. The optical plane was moved 15 μm between z sections.

Bright field experiments were performed on a Leica DMIRBE inverted microscope using a Photron SA3 high speed CMOS camera (Photron, San Diego, CA) and water immersion objective (Leica 20X, NA 0.7). Image sequences were acquired at a frame rate of 150 frames per second.

ZF Treatments

Verteporfin (5 μM) (Sigma Aldrich) and XAV939 (10 μM) were diluted in fish tank water with 0.0033% PTU, in which larvae were incubated in darkness at 28.5°C for the required time.

ZF Immunofluorescence

Embryos were fixed at the desired stages in 4% paraformaldehyde (PFA) overnight at 4°C. After washing in 0.1% PBS Tween 20, embryos were permeabilized in 0.5% PBS Triton X-100 for 20 min at room temperature (RT). Samples were washed and then blocked (3% albumin from bovine serum (BSA), 5% goat serum, 20 mM MgCl2, 0.3% Tween 20 in PBS) during 2h at RT. Primary antibodies were added in the blocking solution and incubated overnight at 4°C. Secondary antibodies were added in 0.1% PBS Tween20 after thorough washing and incubated overnight at 4°C. Embryos were washed and incubated with DAPI (Invitrogen), 1:1000, for 15 min at RT. After being thoroughly washed, samples were mounted for imaging on a Leica SP8 confocal with a dipping immersion objective (Leica HCX IRAPO L, 25X, N.A. 0.95). Z stacks were taken every 10 μm. 3D images were reconstructed using IMARIS software (Bitplane Scientific Software). The ventral pericardium was digitally removed to provide a clearer view of the heart.

Antibodies used were as follows: anti-myosin heavy chain (MF20, DSHB) 1:20, anti-GFP (AVES) 1:500, anti-phospho-Smad 1/5 (Ser463/465) (Cell signaling) 1:50, anti-Islet1 (Genetex) 1:100, anti-Yap1 (Lecaudey laboratory) 1:200. Secondary antibodies: goat anti-chicken Alexa Fluor 488 IgY (H+L) (*In vitro*gen), goat anti-mouse IgG Cy3 conjugate (H+L) (Life technologies) and goat anti-rabbit Alexa Fluor 647 (ThermoFisher) were used at 1:500.

To test the effects of Verteporfin treatment, embryos were rinsed in fish tank water before being fixed and processed as described above.

In Situ Hybridization (ISH)

ISH was performed in whole embryos according to Thisse and Thisse, 2008, with minor modifications. Antisense mRNA probe used was against full coding sequence of *bmp4*. To test the effects of Verteporfin and XAV939 treatments, embryos were rinsed in fish tank water before being fixed and processed as described above.

Whole Mount Immunofluorescence in the Mouse

Embryos were fixed in paraformaldehyde. The cardiac region was dissected, permeabilized in 0.75% Triton. Aldehydes were quenched with 2.6mg/ml NH4Cl. Immunostaining was performed in 10% inactivated horse serum, 0.5% Triton with a primary antibody against Wt1 (Santa Cruz sc-192, 1:50), and with Alexa Fluor conjugated secondary antibodies (1:300) and counterstained with Hoechst (1:400). 80% glycerol was used to make the samples transparent.

Immunofluorescence on Cryosections in the Mouse

Embryos were embedded in 7% gelatin, 15% sucrose, frozen in cold isopentane and sectioned on a cryostat (10 μm). Immunostaining was performed on cryosections as described above, with permeabilization in 0.5% Triton, and with an additional incubation in 0.2 mg/mL goat anti-mouse IgG Fab fragment to reduce non-specific reactivity of antibodies raised in the mouse. Primary antibodies against Tbx18 (Santa Cruz sc-17869, 1:100), Wt1 (Santa Cruz sc-192, 1:50), Yap1 (Santa Cruz sc-101199, 1:100), Amotl1 (Sigma HPA001196, 1:50) and p-Smad1/5/9 (Cell signaling 13820, 1:250) were used, with Alexa Fluor conjugated secondary antibodies (1:500) and Hoechst nuclear counterstaining (1:1000). Samples were imaged in DAKO mounting medium on a LSM700 (Zeiss) confocal microscope with a 40X/1.3 objective. Z stacks were taken every 0.9 μm.

Cell Culture, siRNAs and Transfection

Cells were cultured in appropriate conditions: MDCK (MEM Eagle - Earle's BSS, 10% FCS, AANE 0.1 mM, Sodium Pyruvate 1mM, Gentamicin 40 μg/ml), HeLa (DMEM 4.5 g/l glucose, 10% FCS, Penicillin 100 UI/ml, Streptomycin 100 μg/ml), HEK293 cells (DMEM 1g/L glucose, FCS 10%, Penicillin 100 UI/ml, Streptomycin 100 μg/ml) and DLD-1 (DMEM 4.5 g/l glucose, 10% FCS, Penicillin 100 UI/ml, Streptomycin 100 μg/ml). siRNA (Dharmacon) ON-Target plus - Control pool Non-targeting (D-001810-10-05) and SMART pool human IFT88 (L-012281-01) were used at 50 nM working concentration. Cells were transfected 16h after splitting using Opti-MEM medium and Oligofectamine reagent.

Generation of DLD-1 IFT88-AID Targeted Cells

DLD-1 IFT88-AID cells were generated by adding an AID tag followed by a YFP tag at the 3′ end of the last exon on the IFT88 genomic locus. In detail, a clonal population of DLD-1 cells stably expressing TIR1-9xMyc protein was used for targeting (Holland et al., 2012). sgRNA targeting two regions adjacent to the 3′ end of IFT88 gene were introduced under the control of U6 transcription promoter into two separate vectors encoding for the expression of the Cas9 nickase (D10A) (Cong et al., 2013) (addgene 42335). A donor construct containing ≈600 bp recombination arms surrounding the 3′ end of IFT88 locus, in frame with a sequence encoding for an AID-YFP-Stop sequence, was generated. All three vectors were transfected into DLD-1 TIR1 cells using Xtreme Gene 9 DNA transfection reagent (Roche). Cells were sorted based on their YFP fluorescence and single clones were isolated. Homozygous targeted clones were identified by PCR. Targeting of IFT88 and degradation of IFT88-AID-YFP was confirmed by immunoblot following addition of Auxin (Sigma-Aldrich) at 500 μM in the culture medium for the indicated times.

Immunofluorescence on Cells

Cells were fixed in 100% MeOH for 6 min at −20°C (Ift88 and γ-tubulin antibodies), in 4% PFA for 7 min at RT (DLD-1 cells. Yap1 antibody) or in PFA 4% for 17 min at RT (MDCK and HeLa cells. Yap/Taz antibody). After washing in 0.1% PBS Tween20, cells were permeabilized in 0.5% PBS-NP40 and blocked in 5% BSA 1h at RT. Primary antibodies were added in the blocking solution and incubated overnight at 4°C. Secondary antibodies were added in 0.1% PBS Tween20 after washing and incubated for 2h at RT. Then cells were incubated with DAPI (Invitrogen), 1:1000, for 15 min at RT. After being thoroughly washed, samples were mounted for imaging on a Leica SP5 (siRNA experiments) or SP8 (DLD-1 experiments and experiments to assess subcellular localization) confocal microscope with an oil immersion objective (Leica HCX PL APO lambda blue, 63X, N.A. 1.4). Z stacks were taken every 1 μm.

Antibodies used were as follows: anti-γ-tubulin (Santa Cruz) 1:500, anti-α-tubulin (Sigma, 1:2000), anti-IFT88 (Euromedex) 1:50, anti-Yap1 (4912) (Cell signaling) 1:50 (DLD-1 experiments), and anti-Yap/Taz (D24E4) (Cell signaling) 1:50 (MDCK and HeLa siRNA experiments). Secondary antibodies: goat anti-mouse IgG Cy3 conjugate (H+L) (Life technologies) and goat anti-rabbit Alexa Fluor 647 (*In vitro*gen) were used at 1:500.

Lysates and Immunoblotting

DLD-1 cell extracts were obtained after lysis with Laemmli sample buffer of an equal number of cells for each sample. Proteins were resolved by SDS-PAGE, transferred to nitrocellulose membranes and revealed by immunoblot using Western Lightning Plus-ECL kit (PerkinElmer).

IMMUNOPRECIPITATION (IP) ASSAYS

HEK293 Cells

HEK293 cells (Q-BIOgene AES0503) were co-transfected with plasmids Flag-Amotl1 (Pei et al., 2010) and Ift20-GFP (Follit et al., 2006), or a Flag-control plasmid using Lipofectamine® 2000 Transfection Reagent (ThermoFisher SCIENTIFIC) and cultured for 48h. Proteins were extracted in a lysis buffer (10mMTris-Cl pH 7.5, 5mM EDTA, 150mM NaCl, 10% glycerol and 5% CHAPS) in the presence of protease inhibitors (cOmpleteTM Protease Inhibitor Cocktail, Roche). Immunoprecipitation of protein extracts was performed using a monoclonal anti-Flag antibody covalently attached to agarose (Anti-FLAG M2 Affinity gel, Sigma). Proteins were eluted in 2xNuPAGE LDS Sample Buffer (ThermoFisher). Proteins were separated on SDS–polyacrylamide gel electrophoresis and transferred to a nitrocellulose membrane. Proteins were detected with the primary antibodies against Flag (1:1000, Sigma

F7425), GFP (1:1000, ThermoFisher CAB421), Ift20 (1:500, Proteintech, 13615-1-AP), Yap1 (1:1000, Cell Signaling 4912S) and Amotl1 (1:1000, Sigma HPA001196), followed by HRP-conjugated secondary antibodies (1:5000, Jackson ImmunoResearch) and the ECL detection reagent.

HeLa Cells

We performed IPs using GFP-Trap (ChromoTek) agarose beads in two conditions: Control IP (YAP1-Myc (Boin et al., 2014), pEGFP-C1 and HA-Amotl1 (Ragni et al., 2017)) and IFT88 IP (YAP1-Myc, IFT88-GFP (He et al., 2014) and HA-Amotl1). HeLa cells (2x 10cm dish/ condition) were transfected with Lipofectamine 2000. Experiments were performed using the following setup: Cells were seeded at high density into 10cm dishes and transfected 16 hr after seeding at 95% confluency. Twenty-four hours post-transfection, cells were seeded into 15cm dishes in order to achieve culture of isolated cells (10x 15cm dish/ condition). Proteins were extracted 60 hr post-transfection in a lysis buffer (10mM TrisHCl, pH7.5; 150mM NaCl; 0.5mM EDTA; 0.5% NP-40; protease inhibitors Complete). GFP beads were washed once in lysis buffer and incubated with 16 mg of the protein lysate for 16 hr at 4°C. Beads were washed four times in buffer without detergent and proteins were eluted by boiling for 10 mins. The input (1%) and IP were analyzed using immunoblot and the membranes were probed with anti-GFP (Abcam), anti-Yap/TAZ (D24E4, Cell Signaling) and anti-HA (Sigma Aldrich) antibodies.

ZF avcPE Cell Quantification

We performed whole-mount immunofluorescent staining on control and mutant embryos in the *epi:GFP* reporter line background and imaged the heart using a confocal microscope with a z-step of 10 μm. The different tissues were labeled using anti-myosin heavy chain (MHC) (myocardium) and anti-GFP (*epi:GFP*) antibodies, and DAPI dye to stain for nuclei. We then manually quantified the number of avcPE cells per z slice. We identified the avcPE clusters anatomically: avcPE clusters form in the dorsal pericardium, close to the atrio-ventricular canal (avc). PE cells were identified by their rounded morphology in conjunction with their expression of GFP (although some pericardial cells are also GFP-positive, they can be excluded due to their flat morphology). In order to count each cell only once in the z stack, we only counted a cell when its nucleus was visible.

ZF Myocardial Cell Quantification

We performed whole-mount immunofluorescent staining on control and mutant embryos using anti-myosin heavy chain (MHC) (myocardium) antibody and DAPI dye (nuclei). We imaged the heart using a confocal microscope with a z-step of 10 μm. We then manually quantified the number of myocardial cells per z slice (nuclei surrounded by MHC signal).

Mice PE Volume Analysis

Whole mount embryos stained with Wt1 antibody (Santa Cruz) were scanned on TCS SP8 DLS (Digital Light Sheet) Leica with a water immersion objective (HC APO L, 10X, 0.3). Z stacks were taken every 2 μm. Both, coronal and sagittal views were acquired, if possible, for a more precise analysis (Figure S2F). Using MATLAB software, the contour of the PE was manually drawn (Wt1 signal) for each z plane and the area (A) was calculated. Volume (V) was estimated as:

$$V = \Sigma zn\ Ai \times dz\ ;\ i = 1\ ;\ zn = \text{number of planes};\ dz = 2\ \mu m$$

We performed a double-blind quantitative analysis. 3D images were reconstructed using IMARIS software (Bitplane Scientific Software).

Mice Yap1- and Amotl1-Positive Cell Quantifications

Nuclei positions on the slides were defined using IMARIS (Bitplane Scientific Software) Spots detection function. The results were manually corrected if needed. Nuclei positions were exported from Imaris and imported to MATLAB. Each cell was assigned a unique index. The intensity of Tbx18 signal was evaluated in correspondence with the nuclei positions. Cells where the intensity was found higher than a threshold were considered positive. The threshold was established according to the background noise intensity. Results were manually corrected if needed and Tbx18-positive cells were automatically counted. Yap1 signal was visualized in fire LUT to facilitate perception of signal intensity. Nuclear Yap1-positive cells (higher signal in the nucleus than in the cytoplasm) were manually defined through index identification of cells and counted automatically. The same procedure was followed for Amotl1 signal. The outline of the outer PE region was manually drawn and areas of the two regions were calculated automatically. MATLAB provided the total positive cell number for each signal and area, including signal co-localization. We performed a double-blind quantitative analysis.

Nuclear Yap Quantifications on Cells

Analyses were performed using Fiji (Schindelin et al., 2012). Nuclei areas were selected manually using DAPI signal as reference on z-projection images (sum slices for DLD-1 experiment and maximum intensity projection for siRNA experiments). Yap average nuclear signal intensity was measured for the selected areas. In experiments in DLD-1 cells the values were measured for each individual nucleus, while in the case of siRNA experiments, all the nuclei in a slice were measured together. Values were normalized to their controls in order to merge data from different experiments.

Nuclear/cytoplasmic Yap1 Ratio

Analyses were performed using Fiji. Nuclei areas were selected manually using DAPI signal as reference on z-projection images (sum slices). Cytoplasmic areas were selected using α-tubulin signal as reference. Yap average nuclear signal intensity was measured for the nuclear ROI. Yap average cytoplasmic signal intensity was measured after subtracting nuclear ROI from the cytoplasmic ROI.

QUANTIFICATION AND STATISTICAL ANALYSIS

We applied D'Agostino & Pearson and Shapiro-Wilk normality tests to assess whether the samples fit a normal distribution and F test to compare variances. For normal distributed and homoscedastic samples, we used t test or ANOVA. For non-parametric samples, we applied Man-Whitney or Kruskal-Wallis. The pertinent statistical analyses for each experiment were performed using GraphPad Prism 7 software. For the analysis of nuclear p-smad 1/5/9 and YAP1 signal in mice we used the non-parametric Chi-square test of homogeneity to test whether the observed frequency of positive nuclei was equally distributed across the *wild-type* and mutant embryos. In each figure legend is stated the number of embryos (n), as well as the meaning of error bars and p values.